An Attempt to Study Stability of Stratified Flow Using Smoothed Particle Hydrodynamics

Submitted in partial fulfillment of the requirements

of the degree of

Bachelor of Technology and Master of Technology

by

Arpit Agarwal

(*Roll no.* 10D100008)

Supervisors:

Prof. Amitabh Bhattacharya

&

Prof. Prabhu Ramachandran

Department of Mechanical Engineering

Indian Institute of Technology Bombay

2015

Dissertation Approval

This dissertation entitled **"An Attempt to Study Stability of Stratified Flow Using Smoothed Particle Hydrodynamics"**, submitted by Arpit Agarwal (Roll No. 10D100008), is approved for the award of degree of Bachelor of Technology and Master of Technology in Mechanical Engineering.

Examiners

Prof. Atul Sharma _____ 30/6/15

Prof. Ratul Dasgupta _____ 30/06/2015

Prof. Rochish Thaokar _____ 30/6/15

Supervisors

Prof. Amitabh Bhattacharya _____

Prof. Prabhu Ramachandran _____

Date: 22 June 2015

Declaration of Authorship

I declare that this written submission represents my ideas in my own words and where others' ideas or words have been included, I have adequately cited and referenced the original sources. I also declare that I have adhered to all principles of academic honesty and integrity and have not misrepresented or fabricated or falsified any idea/data/fact/source in my submission. I understand that any violation of the above will be cause for disciplinary action by the Institute and can also evoke penal action from the sources which have thus not been properly cited or from whom proper permission has not been taken when needed.

Signature: Arpit

Arpit Agarwal

10D100008

Date: 22 June 2015

Abstract

Solution of problems involving fluid and flow discontinuities using Smoothed Particle Hydrodynamics is considered. In particular, instability of interfaces under a velocity discontinuity (Kelvin–Helmholtz instability) and viscosity discontinuity are considered in depth. SPH has not yet been used for core-annular flows, this study identifies the problems associated with the same and attempts to solve some of them. A viscosity-stratification model is proposed and tested for simple cases. A serious issue identified is that of particle mixing at the interface. Viscosity and surface tension are employed to alleviate the problem in KHI but there is no universal solution. Sensitivity of the problems to the initialisation is established, the currently employed techniques are assessed, and a general strategy for initialising problems is attempted.

Index terms: smoothed particle hydrodynamics (SPH); Kelvin–Helmholtz instability (KHI); surface tension; viscosity stratification

Contents

List of Figures

Chapter 1

Introduction

1.1 Motivation & Objective

Transporting oils and emulsions is a major challenge for the processing industry. These fluids have a very high viscosity, which means that pumping them requires a very high pressure head. As a solution, a thin layer of another fluid, typically water, is used to lubricate the flow. Such flows, termed as "Core-Annular Flows", occur in in cylindrical pipes, in which the the core is the highly viscous oil or emulsion, and the annulus is typically water (see figure 1.1). In such a lubricated flow, the pressure head required, and therefore energy loss, is very close to that required for pumping pure water [1].

However, CAFs are also prone to instabilities at their interface. These instabilities arise due to the very high velocity gradient, and the sharp viscosity jump at the interface [2]. The often non-Newtonian behaviour of the core fluid further complicates the physics. The instabilities cause the interfacial perturbations to grow, which eventually brings the core in contact with the pipe wall. As a result, the lubrication effect fails. Thus, understanding the stability of the interface of a Core-Annular Flow is of importance. While linear stability theory can give insights into the growth rate of small interfacial perturbations [2], it is not as useful for predicting the dynamics at large amplitude. Numerical simulations can, on the other hand, play an important role towards understanding the non-linear dynamics of the interfacial disturbances. For instance, stable, large-amplitude interfacial waves, with different axial and azimulthal modes, have been observed in experiments involving CAF

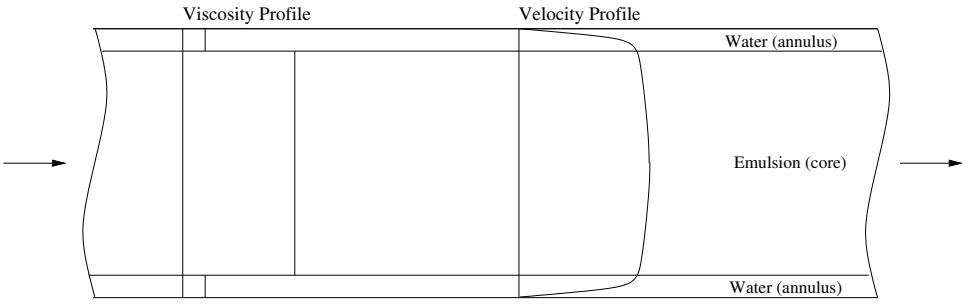

Figure 1.1: Cross section of a core-annular flow situation

[1]. Such large-amplitude waves cannot be explained through linear stability analysis. Our goal here is to investigate such large-amplitude interfacial waves in CAFs using Smooth Particle Hydrodynamics (SPH), which is a numerical method for solving fluid flows. SPH is a relatively new technique, multi-phase flows being an even newer branch. This work is therefore an attempt to understand the ability of SPH to simulate multi-phase flows and fluid instabilities using SPH.

We seek to answer the question of how good SPH currently is at handling these problems, and further, to understand the stability as well as large-amplitude behaviour of the interface with respect to different fluid and flow properties.

1.2 Approach

Since CAF of non-Newtonian fluids have not been simulated in the past, therefore our approach is to validate simple cases (e.g. Kelvin-Helmholtz instability), build SPH models for non-Newtonian fluids, and then attempt simulation of CAF. Our approach therefore involves the following steps:

- Model surface tension, and peform basic tests to validate it (e.g. measure Laplace pressure in a droplet). Surface tension models will be studied in depth here. Surface tension implementations in SPH are relatively new and a lot of the surface tension models used in Eulerean schemes have not yet been implemented in SPH.

- Capture growth rates for a Kelvin–Helmholtz instability (KHI). Simulating KHI has been attempted in the past using SPH. Agertz et al. (2007) in their comparison of SPH and grid based methods have shown that the current SPH schemes do a

poor job of resolving problems like KHI. In his work on modeling discontinuities in SPH [3], Price uses KHI as an example. As his focus is on handling the density and internal energy discontinuity, surface tension effects have not been considered. There have been a couple of other studies of KHI with SPH which do not consider the effects of surface tension. Shadloo et al. [4], [5], [6] have simulated KHI with surface tension and tried to validate it with the analytical results. The plan is to start by reproducing this work and then move on to the aforementioned complexities.

- Model and simulate viscosity difference across the interface using SPH. Viscosity differences have not been traditionally modelled in prior work on SPH. Validate the model using simple cases of Poiseuille and Couette flow.

- Solve stability problem involving viscosity-stratification using SPH. Use other CFD solutions and semi-analytical solutions for validation of the same.

- Attempt a full core-annular flow simulation, study high amplitude behaviour of waves.

1.3 SPH Overview

Broadly speaking, the Navier Stokes equations can be numerically solved in two ways; one is the grid-based method with an Eulerean formulation and the other is a grid-free method with a Lagrangian formulation. Smoothed Particle Hydrodynamics (SPH) is one such grid-free method, with diverse applications. It was developed independently by Lucy (1997) and, Gingold and Monaghan (1997) [7] around the same time for applications in astrophysics. Several reviews, including Monaghan (1992) [8] and Monaghan (2005) [9] have been published since. SPH is very well suited for fluid mechanics problems like free shear flows, solid mechanics problems like explosions, and fractures, where the strains and strain rates are high. Problems involving complicated or dynamic geometries are handled just like any other regular problem in SPH. Also, SPH methods can be readily extended to equations of any dimension.

1.4 Structure of the Thesis

Chapter 2 starts with the description of the 2D problem being considered, the relevant governing equations and their solution using the SPH method. It provides a brief background of the SPH method itself. Chapter 3 is about the implementation of surface tension in SPH, it describes certain popular schemes that are used. The implementation of the surface tension is validated with a few tests and the results are presented. Chapter 4 introduces the current viscosity models used in SPH. Further, chapter 4 describes a model for capturing viscosity stratification. The model is validated against simple stratified 2D Poiseuille and Couette flows. Chapter 5 highlights the problem of accurate initialisation in stability problems. Different methods of initialisation are compared and commented upon in this chapter. In chapter 6 we discuss the different ways of measuring the growth of instability and present results obtained for the different stability problems we considered.

Appendix A presents the linear stability analysis for KHI. Appendix B gives details about the PySPH framework which is used for all the simulations in this thesis. Appendix C describes the origin of certain instabilities in the SPH method itself.

Chapter 2

Numerical Implementation

2.1 Problem Formulation

Two broad types of problems are studied in this work. The physics being solved for is described in brief over here.

2.1.1 Kelvin–Helmholtz Instability

As described in section 1.2, the problem being considered is a simplified form of the actual problem. Two fluids flowing in parallel over each other in opposite directions are considered. Shadloo [4] has considered a square shaped computational domain which has walls on the top and the bottom. To avoid boundary effects the box needs to be periodic in the direction of the flow. The setup represents flow between two moving walls with infinite extent in the wall-parallel directions, see figure 2.1a.

To avoid the complication due to a solid wall, another setup may be considered as shown in figure 2.1b, this does not have walls and instead it is periodic in both directions. Such a setup has been used by Read et al. [10] and Price [3]. Here, there are three parts, the fluid in the centre is sandwiched between layers of fluid flowing in the opposite direction. Thus, periodicity in the vertical direction remains consistent. There are two problems with this setup, firstly, no energy is being added to the flow, in a viscous simulation the fluids will eventually stop, and secondly the effect of gravity cannot be studied as this setup is susceptible to Rayleigh–Taylor instability.

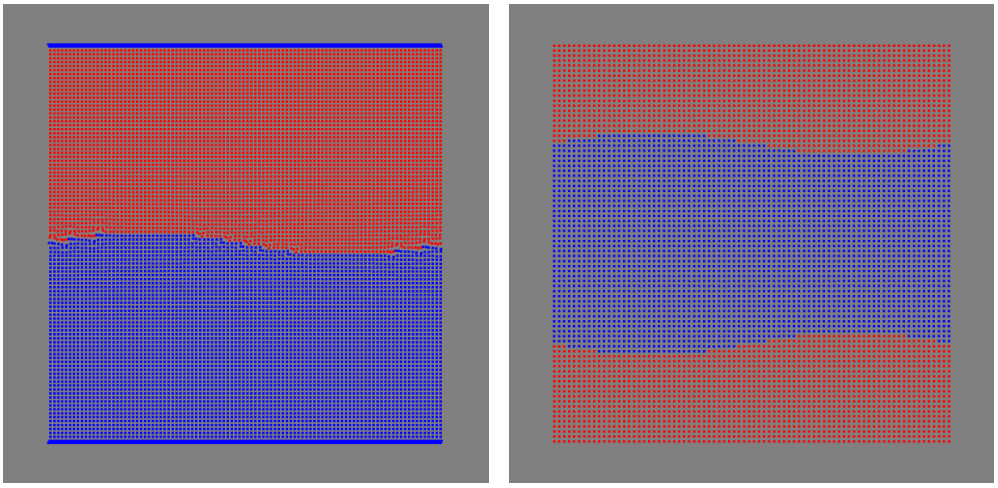

(a) Setup with solid walls (b) Doubly periodic setup

Figure 2.1: The two initial setups

2.1.2 Viscosity Stratified Flow

The problem setup is very similar to the first one descibed in section 2.1.1 (figure 2.1a). The differences being

- Different wavelengths of the initial perturbation were tested. Boxes of different widths (same height) were used in order to get the different wavelengths.
- The relative thickness of the two fluids was changed, i.e the interface position was changed from $y = 0.5$ unit to different values.
- The flow was either driven by a pressure gradient or by the walls, or by both. Fluids were initialised with the fully developed base velocity in such cases.

While the fluid properties and initial conditions are different in the two problems the governing equations remain the same.

2.2 Governing Equations

The governing equations for the fluid are the standard hydrodynamics equations expressed in the Lagrangian form. The SPH method needs to be able to represent these equations to a good approximation.

The inviscid momentum equation is given by

$$\rho\frac{d\mathbf{v}}{dt} = -\nabla p + \rho\mathbf{g}. \tag{2.1}$$

The flow is incompressible, but for the sake of a numerical solution, the standard 'Weakly Compressible' [11][4][12] assumption is made whereby small changes in density are permitted. This brings us to the continuity equation given by

$$\frac{d\rho}{dt} = -\rho\nabla\cdot\mathbf{v}. \tag{2.2}$$

Monaghan [9] has called this equation the *convergence* equation as $-\nabla\cdot\mathbf{v}$ is the opposite of divergence.

To complete the set of equations, a relation for pressure is required. To get the pressure, an equation of state which remains consistent with the weakly compressible assumption is employed. Change in pressure over the background pressure is assumed to be proportional to the change in the density as,

$$p - p_0 = c^2(\rho - \rho_0), \tag{2.3}$$

where c is the speed of sound. c is set so as to keep the density fluctuations to less than 1% [8].

In the presence of surface tension, there is a pressure discontinuity at the interface given by Laplace's formula (3.1). The force due to surface tension is incorporated in the momentum equation, (2.1) then becomes

$$\rho\frac{d\mathbf{v}}{dt} = -\nabla p + \rho\mathbf{g} + \sigma\kappa\hat{\mathbf{n}}\delta_s, \tag{2.4}$$

where σ is the surface tension constant, κ is the interfacial curvature, $\hat{\mathbf{n}}$ is the normal to the interface. The Dirac delta function δ_s ensures that the surface tension term is active only at the interface. This term is explained in detail in chapter 3. There may be an additional viscosity term which has been explained in detail in chapter 4.

2.3 SPH discretization of the equations

In any numerical method, the quantities, their derivatives and integrals are approximately evaluated using values on certain interpolating points. In the Eulerian approach, these points are located on a fixed grid, while in a Lagrangian approach these points move with the fluid.

Initialising the particles

At any time instant, the values of pressure, density, velocity and other relevant fields are assigned at the location of the SPH particles distributed over the domain. These particles are initially setup on a uniformly spaced cartesian grid. Based on their initial positions, the particles belonging to the two phases are identified and assigned the initial properties.

Function Interpolation

To be able to represent differential operators on functions, we need to obtain a smooth representation of these functions over the flow domain. Any function $f(x)$ may be written as:

$$f(x) = \int f(x')\delta(x - x')\mathrm{d}x'. \tag{2.5}$$

Now, if we replace the Dirac delta function with a an approximate Dirac delta function, we get an approximated value of the function. A simple integral interpolant in one dimension, based on a *kernel function*, may be given by

$$\langle f(x)\rangle = \int f(x')W(x - x', h)\mathrm{d}x'. \tag{2.6}$$

Figure 2.2 shows the interpolated function. In order to understand this kernel function better, consider the Taylor series expansion of $f(x')$ inside the integral about x,

$$f(x') = f(x) + \frac{(x' - x)}{1!}f'(x) + \frac{(x' - x)^2}{2!}f''(x) + ... \tag{2.7}$$

substituting this into equation 2.6, we get

$$\langle f(x)\rangle = f(x)\int W(x-x')\mathrm{d}x' + f'(x)\int (x'-x)W(x-x')\mathrm{d}x' + ... \tag{2.8}$$

To get an accurate estimate, we want the integral in the first term to become one and the subsequent terms to vanish, which is essentially

$$\int W(x)\mathrm{d}x = 1 \tag{2.9}$$

$$\int (x)^j W(x)\mathrm{d}x^j = 0, \quad \forall \quad 0 < j \leq k. \tag{2.10}$$

The above approximation is said to be of order k. In theory these are the only conditions on the kernel function. Any function satisfying these properties can be chosen as a kernel function. In practice, the Gaussian function is often chosen for representing the Kernel. Other frequently used forms for the kernel are splines of various orders approximating the Gaussian. h is the 'smoothing length' of the kernel, which, in the case of a Gaussian kernel, is its standard deviation. Naturally, we require

$$\lim_{h\to 0} W(\mathbf{r}, h) = \delta(\mathbf{r}). \tag{2.11}$$

A lot of work has been done on the choice of kernel functions itself, and many variations have been suggested for dealing with accuracy and stability of SPH [13][14].

To interpolate the value of a function at any point in the fluid, the function is represented in terms of its value at the Lagrangian *particles*. m_a, ρ_a and $\mathbf{r}_a$ denote the mass, density and position of particle a respectively. The integral in Eqn (2.5) may be approximated as a summation over these particles. The summation interpolant is given by

$$\langle A(\mathbf{r})\rangle = \sum_b m_b \frac{A_b}{\rho_b} W(\mathbf{r}-\mathbf{r}_b, h). \tag{2.12}$$

As an example, take A as the density, (2.12) then becomes

$$\rho(\mathbf{r}) = \sum_b m_b W(\mathbf{r}-\mathbf{r}', h). \tag{2.13}$$

Note that $\frac{m_b}{\rho_b}$ is representative of the volume, dx.

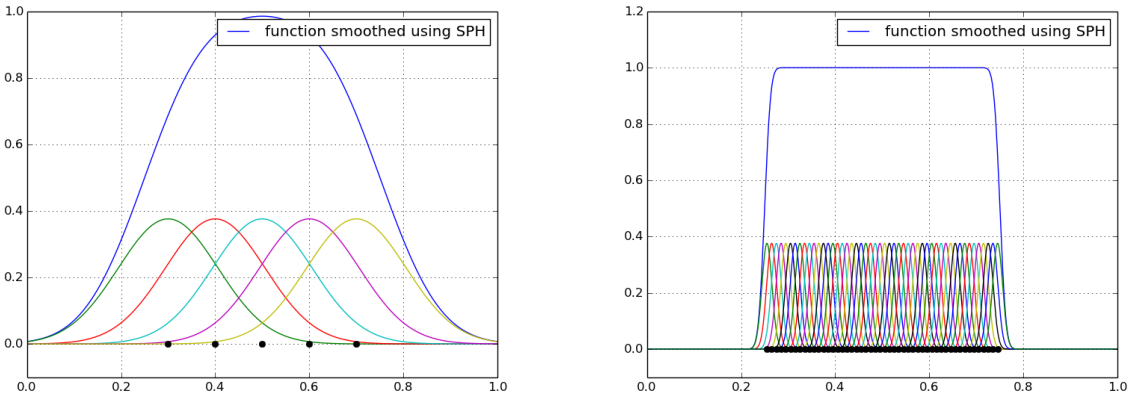

(a) Using 5 particles (b) Using 50 particles

Figure 2.2: Representation of a 1D function which is constant between x=0.25 and x=0.75 using SPH

First Derivatives

Several variations are possible in the derivatives of the SPH approximated functions. These variations are responsible for the wide variety of implementations of the same governing equations.

Equation (2.12) may be differentiated exactly to give

$$\frac{\partial A_s}{\partial x} = \sum_b m_b \frac{A_b}{\rho_b} \frac{\partial W}{\partial x}. \tag{2.14}$$

Note that this is an exact derivative of an approximated function, if A is a constant function, the derivative given by (2.14) does not vanish. To overcome this problem a slightly different approached is used, the derivative is written as

$$\left(\frac{\partial A}{\partial x}\right) = \frac{1}{\Phi}\left(\frac{\partial(\Phi A)}{\partial x} - A\frac{\partial \Phi}{\partial x}\right). \tag{2.15}$$

Now, writing both derivatives using (2.14) we get

$$\left(\frac{\partial A}{\partial x}\right)_a = \frac{1}{\Phi_a}\sum_b m_b \frac{\Phi_b}{\rho_b}(A_b - A_a)\frac{\partial W_{ab}}{\partial x_a}. \tag{2.16}$$

On setting Φ as 1 the expression becomes

$$\frac{\partial A_a}{\partial x_a} = \sum_b \frac{m_b}{\rho_b}(A_b - A_a)\frac{\partial W_{ab}}{\partial x_a}. \tag{2.17}$$

Whereas, if Φ is chosen to be ρ the expression becomes

$$\frac{\partial A_a}{\partial x_a} = \frac{1}{\rho_a}\sum_b m_b(A_b - A_a)\frac{\partial W_{ab}}{\partial x_a}. \tag{2.18}$$

Clearly, the RHS for (2.16) through (2.18) vanish in case of constant A, which resolves the problem in (2.14). This has direct implications on the continuity equation,

$$\frac{d\rho}{dt} = -\rho\nabla\cdot\mathbf{v}. \tag{2.19}$$

It can be written in two forms

$$\frac{d\rho_a}{dt} = \rho_a\sum_b \frac{m_b}{\rho_b}\mathbf{v}_{ab}\cdot\nabla_a W_{ab} \tag{2.20}$$

as per (2.18) and

$$\frac{d\rho_a}{dt} = \sum_b m_b\mathbf{v}_{ab}\cdot\nabla_a W_{ab}, \tag{2.21}$$

as per (2.17), where $\mathbf{v}_{ab} = \mathbf{v}_a - \mathbf{v}_b$. In most cases both equations give similar results, but in case of large density ratios in contact, (2.20) is reported to give better results [9].

Second Derivatives

As in the case of the first derivatives, the second derivatives are generally obtained by differentiating the SPH interpolant twice, for eg.

$$\left(\frac{d^2T}{dx^2}\right)_a = \sum_b m_b T_b \frac{d^2W_{ab}}{dx_a^2}. \tag{2.22}$$

However, this expression is sensitive to particle disorder; better approaches have been suggested [9] which overcome the disadvantages.

2.4 Timestep Values

There are four constraints on the timestep value:

1. CFL: Based on speed of sound waves in the weakly compressible formulation [8] we get
$$\Delta t_s \leq 0.25\frac{h}{c}, \tag{2.23}$$
where c is the numerical speed of sound.

2. Viscosity: Based on the viscous timescale [15] we get
$$\Delta t_\nu \leq 0.125\frac{h^2}{\nu}. \tag{2.24}$$

3. Surface tension: Based on the capillary phase velocity [16] and the CFL condition we get
$$\Delta t_\sigma \leq 0.25\left(\frac{\rho_m h^3}{2\pi\sigma}\right)^{1/2} \tag{2.25}$$
where ρ_m is the mean fluid density (relevant in cases involving fluids of different densities).

4. Particle accelerations: Based on the maximum acceleration, a, of a fluid particle [15] we get
$$\Delta t_a \leq 0.25\left(\frac{h}{a}\right). \tag{2.26}$$

In all the simulations timestep values are chosen by taking the minimum of these values and multiplying an additional safety factor of 0.9, i.e.

$$\Delta t = 0.9\min(\Delta t_s, \Delta t_\nu, \Delta t_\sigma, \Delta t_a). \tag{2.27}$$

Timestep constraints based on surface tension and viscosity are given here for the sake of completeness. A detailed description of models used for the same may be found in Chapters 3 and 4 respectively.

2.5 Solving the equations

The previous sections give the complete set of equations and their discretization over the particles. In practice, the standard formulation for calculating derivatives always gives some problems, the final SPH discretization used is almost always a slight modification of the standard scheme, as shown for the continuity equation by (2.20) and (2.21). A similar manipulation has to be done for the pressure gradient, it is written as

$$\nabla p = \rho \nabla \left(\frac{p}{\rho} \right) + \frac{p}{\rho} \nabla \rho. \tag{2.28}$$

Using this, the momentum equation (2.1) becomes

$$\frac{dv_a}{dt} = -\sum_b m_b \left(\frac{p_a}{\rho_a^2} + \frac{p_b}{\rho_b^2} \right) \frac{\partial W_{ab}}{\partial x_a} + \mathbf{g}. \tag{2.29}$$

As we can see, the equations governing the physics become expressions of inter-particle forces when expressed in the SPH form.

Instead of using the continuity equation (2.2) for evaluating the densities, the 'summation density' is often used, it is given by

$$\rho_a = \sum_b m_b W_{ab}. \tag{2.30}$$

Note that this is just the integral form of the continuity equation (2.2). The minor differences are only apparent in case of high density gradients [3].

In a simple Euler step integration, the following steps are followed to evolve a fluid system starting with an initial distribution:

1. Using the summation density (2.30) on the positions, the density values are calculated.
2. The equation of state (2.3) is used to calculate the pressures.
3. The momentum equation (2.29) is used to calculate the velocities of the particles.
4. The particles are advected with the calculated velocities.

This is a first order scheme, which means that it requires very small time steps for accurate results. Several higher order schemes have been described in literature. Through the course of this work, higher order predictor-corrector [9] schemes have been used.

2.6 Transport Velocity Formulation

Transport-velocity formulation (TVF) [11] is an SPH formulation introduced in 2013 by Adami et al. This method is characterised by different treatment of advection-velocity of particles and the momentum-velocity of particles. The advection-velocity is obtained from the momentum velocity but is corrected for the effect of a constant background pressure.

2.6.1 Motivation

The standard SPH discretisation of the momentum equation (equation 2.29) is not 0th-order consistent in pressure, therefore, the results are dependent on the background pressure. Also, the standard formulation is prone to certain instabilities in the presence of negative pressures (see Appendix C). TVF has been developed to overcome these problems.

2.6.2 Brief explanation

We have a new quantity called the advection-velocity, $\tilde{\mathbf{v}}$. This is the actual velocity used for advecting particles. Material derivative, $\tilde{d}/dt$, is defined using the advection velocity as

$$\frac{\tilde{d}()}{dt} = \frac{\partial()}{\partial t} + \tilde{\mathbf{v}} \cdot \nabla() \tag{2.31}$$

Final form of the momentum equation derived by Adami et al. is

$$\frac{\tilde{d}(\rho\mathbf{v})}{dt} = -\nabla p + \eta\nabla^2\mathbf{v} + \rho\mathbf{g} + \nabla \cdot (\rho\mathbf{v}(\tilde{\mathbf{v}} - \mathbf{v})). \tag{2.32}$$

The transport velocity at each timestep is evaluated as

$$\tilde{\mathbf{v}}_i(t + \delta t) = \mathbf{v}_i(t) + \delta t \left(\frac{\tilde{d}\mathbf{v}_i}{dt} - \frac{1}{\rho_i}\nabla p_b, \right) \tag{2.33}$$

where p_b is the background pressure. Although $\nabla p_b = 0$, SPH discretisation of the term gives a non-zero contribution as per equation 2.29.

Note that background pressure does not feature in the momentum equation, equation 2.32, it does however feature in the advection velocity calculation given by equation 2.33.

2.6.3 Performance

TVF has been shown to be stable to the tensile instability and to give results with better accuracy than the standard SPH formulation [11]. The standard weakly compressible SPH formulation requires small timesteps for stability. A simple test of a static fluid surrounded by walls on all four sides is set up. In any weakly compressible form, there are pressure oscillations which keep reflecting off the walls and hence magnifying. The pressure oscillations rise to a point where they start moving the particles. This reflects as increased kinetic energy of the fluid. Due to the background pressure normalisation, TVF is more stable to this situation.

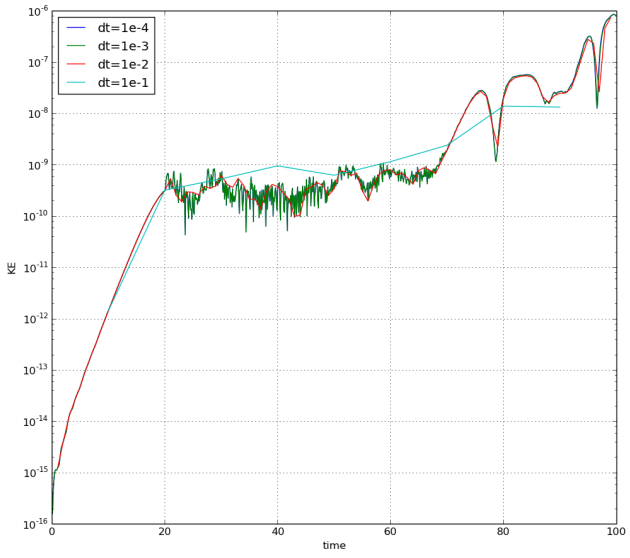

Figure 2.3: Pressure waves instability in TVF

Figure 2.3 shows the total kinetic energy of the fluid against time for a static fluid. As expected, the kinetic energy increases with time, but at a lower rate compared to the standard SPH formulation. Even at $t = 100$ unit, the total kinetic energy is 10^{-6} unit,

which means that there is no visible motion of particles. In case of standard SPH the particles blow-up by $t = 100$ unit even with timesteps as low as $\Delta t = 10^{-4}$ unit. Moreover, in figure 2.3 we see that the performance is the same for Δt values as high as 10^{-1} unit.

TVF involves a slight computational overhead but offers clear advantages over the standard SPH formulation. Throughout this work we have use the Transport Velocity Formulation of SPH unless otherwise mentioned.

Chapter 3

Surface Tension

3.1 Introduction

Whenever there are two immiscible fluids in contact, certain discontinuities exist at the interface. The interface is found to behave like it is under tension, like a stretched balloon. The molecules near the surface experience different attractive forces from different sides of the interface; this imbalanced force on the interfacial molecules leads to surface tension. An important consequence of surface tension is that it leads to a pressure discontinuity whenever the interface has a curvature. When the surface tension coefficient is constant, the expression for this pressure discontinuity reduces to Laplace's formula [17]

$$p_2 - p_1 = \sigma\kappa \tag{3.1}$$

The pressure is higher on the concave side of the interface. This higher pressure will try to 'push out' the interface, thus tending to increase the total surface area of the interface. On the other hand, the surface tension tends to reduce the surface area of the interface. It is the balance between these two effects that leads to Eqn (3.1).

Surface tension forces (or capillary effects) become especially important in flows involving small length scales and large time scales.

3.2 SPH Models

Surface tension forces have been implemented in computational models for multiphase flows in methods such as the volume of fluid (VOF) method, level set (LS) method [18], lattice-Boltzmann method (LBM), and front tracking method (FT). Surface tension modeling in SPH is fairly new, while the first theoretical work in this direction was done around 1995, Morris [15] was the first to report successful simulations in 2000.

Surface tension models in SPH can be broadly classified into two categories, one which models the microscopic inter-phase attractive potentials and the other is a macroscopic surface-tension approach. While the first approach is relatively straightforward, it needs calibration. The formulation is resolution dependant for a given set of parameters, i.e. forces do not converge to a unique value as the resolution is increased. The macroscopic approach, which typically uses an approach called continuum surface force (CSF) [16] avoids this problem. A few models that are based on the macroscopic approach have been summarised here.

3.2.1 Basic CSF Implementation

CSF was developed by Brackbill et al. [16]. Here we study CSF implementations for inviscid incompressible flows, with uniform surface tension. The basic idea of CSF is to interpret surface tension, which is a surface force, as a continuous, 3-D effect across an interface rather than a boundary condition on the interface. It removes problems arising out of complicated topologies. The surface force is converted to a volume force, which in theory acts on the entire bulk of the fluid, to give the desired pressure discontinuity at the interface.

The surface tension force, $\mathbf{F}_s$, is translated to a volume force, $\mathbf{f}_s$, by using a surface dirac delta function δ_s as

$$\mathbf{F}_s(\mathbf{x}, t) = \mathbf{f}_s(\mathbf{x}, t)\delta_s. \tag{3.2}$$

δ_s is a normalised function which peaks at the interface. $\mathbf{f}_s$ is given by

$$\mathbf{f}_s = \sigma\kappa\hat{\mathbf{n}} + \nabla_s\sigma, \tag{3.3}$$

where σ is the surface tension coefficient defined for a pair of fluids, $\hat{\mathbf{n}}$ is the unit normal to the interface, κ is the curvature of the interface and ∇_s represents the surface gradient. The first term in Eqn (3.3) acts normal to the surface while the second term acts tangentially to the surface. The second term in Eqn (3.3) represents the forces that arise out of spatial variation in the surface tension (Marangoni Effect). The first term tries to smooth out regions of high curvatures, thus reducing the surface area of the interface and subsequently the surface energy.

Morris [15] has adapted the CSF formulation to SPH. One of the methods described by him directly uses the curvature, but it does not conserve linear or angular momentum, and may be unstable at a higher resolution. Following is a more detailed description of the method.

Identifying the Interface

We use a colour function, c, to distinguish between the two phases. The colour is different for the two phases and is uniform through a given phase, so there is a colour discontinuity at the interface. Naturally, normals to the interface will be given by the gradient of this colour function, therefore,

$$\mathbf{n} = \frac{\nabla c}{[c]}, \tag{3.4}$$

where $[c]$ is the jump in c across the interface. The interface is automatically tracked by the advection of this colour function. δ_s is used to identify the transitional region, it is chosen to be

$$\delta_s = |\mathbf{n}|. \tag{3.5}$$

Typically, c would be set as 1 and 0 for the two fluids, so $[c]$ becomes 1, in which case

$$\delta_s = |\nabla c|. \tag{3.6}$$

Obtaining the Curvature

The curvature determines the magnitude of the force (3.3), it can be calculated using

$$\kappa = -\nabla \cdot \hat{\mathbf{n}}, \tag{3.7}$$

where $\hat{\mathbf{n}}$ is the unit normal evaluated from $\mathbf{n}$.

SPH discretisation

The normals and the curvatures are evaluated using the standard SPH discretization methods for evaluating the divergences and gradients of functions, as described in Chapter 2.

This formulation has one problem though; large errors occur at the fringes of the transition zone. There, the normals have a small magnitude and may have erroneous directions, see figure 3.3a.

The obvious correction is to eliminate these fringe points from the calculation. This is done by setting a criteria to determine whether a normal is 'reliable' before using it.
insert expression here
ϵ can be chosen as $0.01/h$ as it scales appropriately with the resolution. Now, since we are ignoring some of the normals, we need to appropriately modify (3.7), this is done by using a correction factor $\mathscr{C}$. Figure 3.3b shows the curvature values evaluated with this correction.

Better estimates of the normals are obtained when the colour is smoothed out before the calculations as per

$$c'_a = \sum_b \frac{m_b}{\rho_b} c_b \nabla_a W_{ab} \tag{3.8}$$

Figure 3.3c shows the final result when smoothed colour is used with the aforementioned correction to eliminte the fringe values.

3.2.2 Reproducing Divergence Approximation

Adami et al. [12] proposed a different scheme for handling the curvature calculation. The divergence of a vector field is approximated as

$$\nabla \cdot \Phi_a = d \frac{\sum_b V_b \Phi_{ab} \cdot \nabla_a W_{ab}}{\sum_b V_b \mathbf{r}_{ab} \cdot \nabla_a W_{ab}} \tag{3.9}$$

where d is the number of spatial dimensions and V_b is the volume of particle b.

Another problem which the other methods fail to address was that of high density

ratios. For an air-water like interface, the surface tension force is dominant on the water side. In previous methods the force is uniformly distributed across the interface. This results in the accelerations of air to be 1000 times greater than those of water. This also introduces numerical issues; primarily, the step size for time integration has to be made very small. To tackle this problem, a density weighed colour is used for obtaining the colour gradients.

3.2.3 Another CSF implementation

Clearly, the calculation of the curvature is cumbersome. Morris [15] implemented another method where the surface tension force is derived as the gradient of a tensor. This method conserves linear momentum, but might become unstable at high resolutions. A similar approach is used by Hu et al. [19] for simulating flows with viscosity ratios. He also simulates three-phase interactions with it.

In this approach surface tension force is given by

$$\mathbf{f}_s = \nabla \cdot \Pi \tag{3.10}$$

where the surface stress tensor, Π is given by

$$\Pi = \sigma(\mathbf{I} - \hat{\mathbf{n}}\hat{\mathbf{n}})|\nabla C| \tag{3.11}$$

3.2.4 Interface Tracking

Zhang [20] has implemented a method based on interface tracking for surface tension. Interfacial particles are detected dynamically, lagrangian interpolation polynomials are used to construct the interface locally for each of the interfacial particles. To tackle the problem of a multivalue function, the origin is transformed to the particle before constructing the polynomial. For a 3-D interface, moving least squares method is used. The curvatures are then analytically evaluated.

In a slightly different application by Zhang et al. [21], the boundary particles of the two phases are detected, surfaces are constructed for these sets of particles and then the

midpoints of the lines joining the two surfaces are called interface points. These interface points are used to construct another surface which is used for the curvature calculation, and then the force is then transferred to the boundary particles.

3.3 Results: Testing the surface tension models

Calculating the surface tension forces is a multi-step process, the errors introduced at any step carry forward. To check the correctness of the intermediate quantities certain tests are conducted, the results of which are presented here.

3.3.1 Circular Droplet Test

This is a static test problem. As shown in figure 3.1, a circular droplet of one phase is placed in a square domain containing another phase.

Capturing the interface & curvature

Figure 3.2 shows the surface dirac delta function. It becomes maximum at the interface and drops to zero away from the interface. The calculation is done along a horizontal line passing through the centre of the circular droplet. The interface on the left side is shown. The area under the curve is very close to 1, as required.

Figure 3.3 shows the calculated curvature values for the interfacial particles. The formulation described in section 3.2.1 is tried out. Again, the calculation is done along a horizontal line passing through the centre of the circular droplet. The solid lines are $y = 1/r$ lines, where r is the distance from the centre of the droplet, they give the analytically expected value of the curvature.

Clearly, the final form with the correction and smoothing gives the best results, it is used for all further simulations.

3.3.2 Square Droplet Test

This is a dynamic test for surface tension for verifying the nature of the final surface tension force. A square droplet is set up in a square domain containing a different phase.

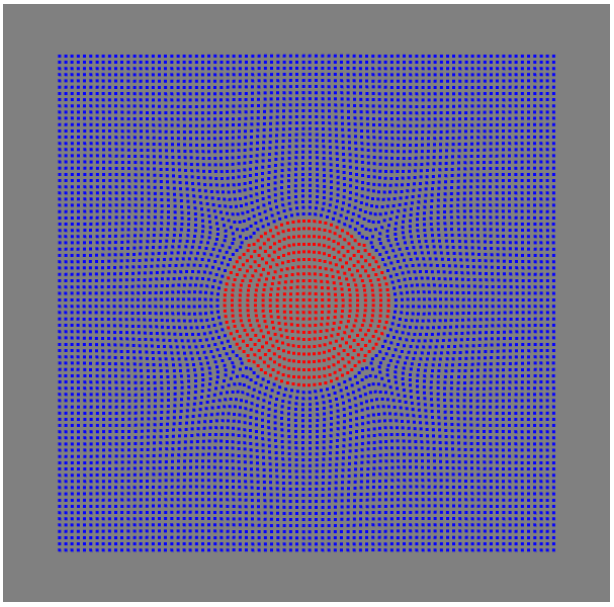

Figure 3.1: Circular droplet setup

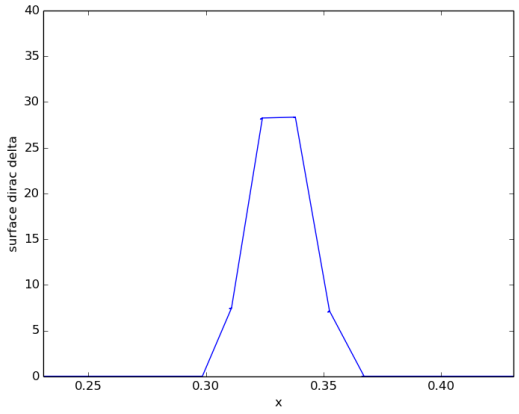

Figure 3.2: Surface dirac delta function along the centreline

This system is allowed to evolve under the surface tension force, see figure 3.4.

At the corners of the square the curvature is high, while, away from the corners, the curvature is low. Therefore, it is expected that the corner particles will move inwards, leading to a circular shape for the droplet. This is consistent with the nature of surface tension forces, whereby they try to reduce the interfacial area.

The droplet is expected to oscillate, and therefore viscosity is used as a damping force in the test shown here. In the absence of viscosity the droplet keeps oscillating, the interface eventually breaks, and the particles mix. The test case shown in figure 3.4 uses a viscosity [11] to damp the oscillations.

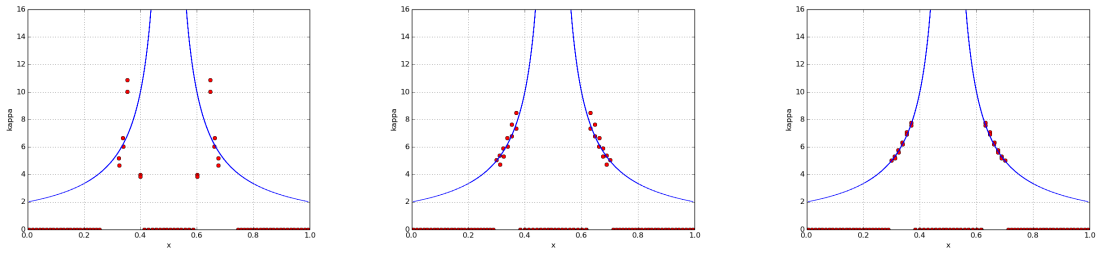

(a) Basic (b) Basic with correction (c) Smoothing & correction

Figure 3.3: Curvature values by the different models

Figure 3.5a shows the pressure field in the final equilibrium state of the system. Figure 3.5b shows the pressure values along the centreline. The solid line gives the expected pressure values in accordance with Laplace's formula (3.1). The obtained pressure values do not exactly follow the analytical value. This is due to the fact that there are pressure waves of small amplitude in the domain, because of the weakly compressible formulation used. The time averaged pressure values fit the curve better (not shown here).

3.3.3 Comments

Even though the simple test cases seem to give reasonable results, there are problems with the implementation of surface tension. If, due to some reason, a particle leaves the interface and enters the other phase, then the region surrounding it is also considered as an interface and forces are applied on it. Moreover, the curvature of such an interface is very high, which leads to a high surface tension force. So, even a slight diffusion of the interface leads to spurious accelerations. Smoothing the colour field gives better results in such cases, but it does not completely eliminate the problem.

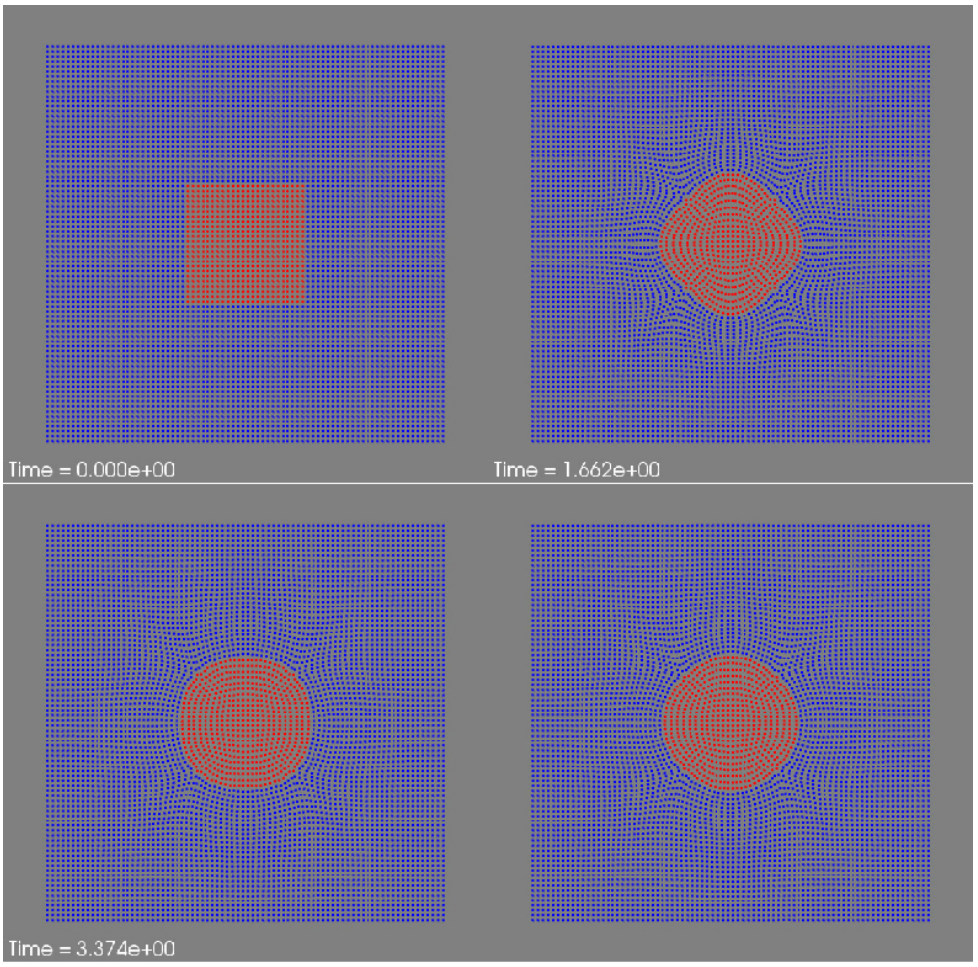

Figure 3.4: Damped oscillation of an initially square droplet

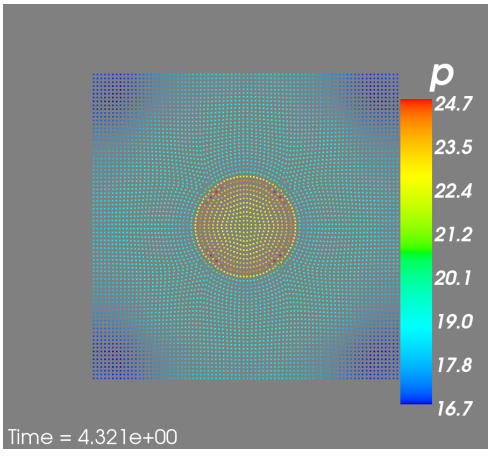

(a) 2D domain

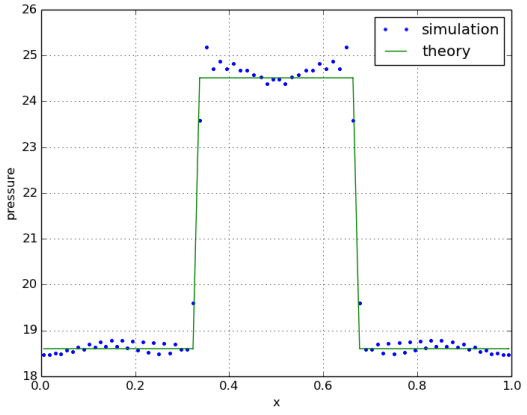

(b) Along the centreline

Figure 3.5: Pressure discontinuity across the interface

Chapter 4

Viscosity

Viscosity plays an important role in the fluid momentum equation. In several applications layers of fluids with different viscosities come in contact with each other. The viscosities of the fluids often differ by several orders of magnitude [22]. It is therefore essential to capture the effect of viscosity and discontinuities in viscosity accurately.

4.1 Viscous force term

The total stress in a moving fluid may be split into two parts: the isotropic part and the anisotropic part. For an incompressible Newtonian fluid the total stress may be expressed as

$$\tau_{ij} = -p\delta_{ij} + 2\mu e_{ij}, \tag{4.1}$$

where p is the pressure, μ is the coefficient of viscosity and e_{ij} is the strain rate given by

$$e_{ij} = \frac{1}{2}\left(\frac{\partial u_i}{\partial x_j} + \frac{\partial u_j}{\partial x_i}\right). \tag{4.2}$$

Therefore, the viscous stress is given simply by

$$\sigma_{ij} = \mu\left(\frac{\partial u_i}{\partial x_j} + \frac{\partial u_j}{\partial x_i}\right). \tag{4.3}$$

The fluid momentum equation is

$$\rho \frac{d\mathbf{u}}{dt} = -\nabla p + \nabla \cdot \tilde{\sigma} + \mathbf{f}_b. \tag{4.4}$$

In case of a uniform viscosity, the viscous force term

$$\nabla \cdot \tilde{\sigma} = \nabla \cdot (\mu \nabla \mathbf{u}), \tag{4.5}$$

reduces to

$$\nabla \cdot \tilde{\sigma} = \mu \nabla^2 \mathbf{u}. \tag{4.6}$$

The viscous force term is tricky to evaluate due to the presence of second derivatives. There are several SPH formulations which are discussed below.

4.2 Typical SPH implementations

Basa et al.[23] have reviewed different viscosity implementations and labelled five viscosity implementations in SPH as models A-E. The models have been investigated and it is found that each of them have their advantages and disadvantages.

4.2.1 Model A: Direct derivatives

Model A is the most intuitive way of modelling the viscous stress term. Second derivatives of the velocity field are evaluated directly form the SPH interpolated $\mathbf{u}$ field as

$$\langle \nabla^2 \mathbf{u} \rangle = \sum_b \frac{m_b}{\rho_b} \mathbf{u}_b \nabla_a^2 W_{ab}. \tag{4.7}$$

A disadvantage of this model is that accuracy drops with disordering of particles.

4.2.2 Model B: Two-pass derivatives

Model B involves the nesting of two first derivatives in order to obtain a second derivative. The first derivative is evaluated in one pass over the particles, and a derivative of this

first derivative field is evaluated in the second pass.

$$\langle \nabla^2 \mathbf{u} \rangle = \langle \nabla \cdot \nabla \mathbf{u} \rangle = \sum_b \frac{m_b}{\rho_b} \left(\sum_b \frac{m_b}{\rho_b} \mathbf{u}_b \nabla_a W_{ab} \right) \cdot \nabla_a W_{ab} \tag{4.8}$$

A disadvantage of model B is that it is computationally expensive. It gathers information from twice the area (In case of a ghost-particle BC implementation (see section 4.3) twice the number of ghost particles are required).

4.2.3 Models C, D, E: Mixed finite-difference/SPH approximation

These three models combine a finite-difference and an SPH derivative. There is term equivalent to $(\mathbf{u}_a - \mathbf{u}_a)/(\mathbf{r}_a - \mathbf{r}_b)$, which is a finite-difference derivative, and there is a ∇W_{ab} term, which is the SPH derivative. This was first proposed by Monaghan and Gingold [8] as an artificial viscosity term not meant to model physical viscosity. The artificial viscosity is given by

$$\frac{d\mathbf{u}_a}{dt}_{visc} = -\sum_b m_b \Pi_{ab} \nabla_a W_{ab} \tag{4.9}$$

where

$$\Pi_{ab} = \begin{cases} \frac{-\alpha 0.5(c_a + c_b)\mu_{ab} + \beta \mu_{ab}^2}{0.5(\rho_a + \rho_b)}, & \text{if } \mathbf{v}_{ab} \cdot \mathbf{r}_{ab} < 0. \\ 0, & \text{otherwise.} \end{cases} \tag{4.10}$$

The μ_{ab} term is a combination of a finite-difference derivative with an SPH derivative of velocity given by

$$\mu_{ab} = h \frac{\mathbf{u}_{ab} \cdot \mathbf{r}_{ab}}{r_{ab}^2 + \eta^2}, \tag{4.11}$$

where $\mathbf{u}_{ab} = \mathbf{u}_a - \mathbf{u}_b$, $\mathbf{r}_{ab} = \mathbf{r}_a - \mathbf{r}_b$ and η is a small parameter.

Models C and D differ only slightly in their form. Model C is given by

$$\langle \frac{1}{\rho} \nabla \cdot \tilde{\sigma} \rangle_a = \sum_b m_b \frac{8}{\rho_a + \rho_b} \left(\frac{\mu_a}{\rho_a} + \frac{\mu_b}{\rho_b} \right) \frac{\mathbf{u}_{ab} \cdot \mathbf{r}_{ab}}{r_{ab}^2 + \eta^2} \nabla_a W_{ab}, \tag{4.12}$$

and model D is given by

$$\langle \frac{1}{\rho}\nabla \cdot \tilde{\sigma} \rangle_a = \sum_b m_b \frac{\zeta}{\rho_a \rho_b} \frac{4\mu_a \mu_b}{(\mu_a + \mu_b)} \frac{\mathbf{u}_{ab} \cdot \mathbf{r}_{ab}}{r_{ab}^2 + \eta^2} \nabla_a W_{ab}, \tag{4.13}$$

where ζ is a problem specific parameter. Morris et al. [15] proposes a slightly different model E which is given by

$$\langle \frac{1}{\rho}\nabla \cdot \tilde{\sigma} \rangle_a = \sum_b m_b \frac{(\mu_a + \mu_b)}{\rho_a \rho_b} \frac{\mathbf{r}_{ab} \cdot \nabla W_{ab}}{r_{ab}^2} \mathbf{u}_{ab}. \tag{4.14}$$

The most significant difference between models C, D and model E is that in E the force is aligned with the relative velocity of particles while in C and D it was aligned with the line joining the particles ($\nabla_a W_{ab}$ is radial in direction as W_{ab} is spherically symmetric).

Models C and D conserve both linear and angular momenta. This is because the terms are symmetric in a and b, and the force acts along the line joining the particles. Model E is also symmetric in a and b, but the force acting on particle a due to particle b is not collinear with the force acting on particle b due to particle a. Therefore, while model E conserves linear momentum it fails to conserve angular momentum.

Basa et al. have shown models D and E to be superior to the other models with respect to robustness and accuracy. However, model D requires a case-specific parameter which is a serious drawback. Hence, we have used model E (and its variations) in this work.

4.3 No-slip wall boundary condition

Particles at the edge of a fluid domain have neighbouring fluid particles only on one side. Only these particles contribute to the inter-particle interactions. This one sided contribution gives incorrect function 'interpolations'. This effect can be seen in the 1D domain represented in figure 2.2. The particles can be interpreted to be fluid particles held between two walls and the function being represented could be any flow/fluid property (e.g. ρ). As the particles at near the edge of the domain have support only on one side, the interpolation function drops in value near the edge as is clearly seen in the figure.

There are several wall boundary condition implementations in SPH. They may be

broadly classified into two types. In the first model the walls are filled with boundary particles which ensure kernel support for fluid particles that come close to the boundary. In the second model repulsion forces are introduced on fluid particles in order to avoid wall penetration. Liu and Liu have also described a hybrid of the two methods in their review paper [24].

While the first approach is intuitive and easy to implement, it requires wall particles which are several layers thick (depending on the kernel function and the smoothing length used). The second approach requires only a single layer of boundary particles.

In this work a wall treatment proposed by Adami et al. [25] is employed. Dummy wall particles are used to model the interface between fluid and solid. A no-slip condition can be imposed by an appropriate choice of wall velocities for viscous interaction between fluid and wall particles.

To impose a no-slip condition, firstly the fluid velocity is extrapolated onto the wall particles as

$$\tilde{\mathbf{v}}_a = \frac{\sum_b \mathbf{v}_b W_{ab}}{\sum_b W_{ab}} \tag{4.15}$$

where 'b' is the set of fluid particles neighbouring wall particle 'a'. Then, the velocity of the wall particle is set as

$$\mathbf{v}_w = 2\mathbf{v}_a - \tilde{\mathbf{v}}_a, \tag{4.16}$$

where $\mathbf{v}_a$ is the physical wall velocity. This method does not require any information about the geometry of the boundary once the wall particles are initialised.

Note that a free-slip condition may be implemented by simply turning off viscous interaction between fluid and wall particles.

4.4 Discontinuous Viscosity

There are several multiphase fluid flows for which a large viscosity jump can exist within the fluid. The simplest example of such a case would be the flow of binary immiscible fluids like oil and water. It is important to model this viscosity discontinuity appropriately in order to obtain correct velocity profiles which satisfy the shear-stress balance condition in the governing differential equations at the interface.

To the best of our knowledge there has not been any study of viscosity stratified flows using SPH. We have adapted a conduction model proposed by Cleary and Monaghan [26] used for heat transfer in materials with discontinuous properties to viscosity stratification.

Diffusion of thermal energy via heat conduction is analogous to diffusion of velocity via viscous interaction. They both follow gradient diffusion laws. For conduction in an incompressible solid the energy equation is

$$\rho c \frac{dT}{dt} = \nabla \cdot (k \nabla T) \tag{4.17}$$

where c is the specific heat and k is the thermal conductivity. The right hand side of equation 4.17 is analogous to equation 4.5. Viscosity, μ, is replaced with thermal conductivity, k, and velocity, $\mathbf{u}$, is replaced with temperature, T. The boundary condition to be satisfied in the two cases is heat flux balance and shear stress balance.

In case of uniform thermal conductivity equation 4.17 in the SPH form is given by

$$\rho c \frac{dT}{dt} = \sum_b \frac{m_b}{\rho_a \rho_b} 2k T_{ab} \frac{|\nabla_a W_{ab}|}{r_{ab}}. \tag{4.18}$$

Cleary and Monaghan [26] have derived a form of the diffusion term which satisfies heat flux balance across the interface given by

$$\rho c \frac{dT_a}{dt} = \sum_b \frac{m_b}{\rho_a \rho_b} \frac{4 k_a k_b}{k_a + k_b} T_{ab} \frac{|\nabla_a W_{ab}|}{r_{ab}}, \tag{4.19}$$

effectively replacing the thermal conductivity, k, in eqn. 4.18 with the harmonic mean of thermal conductivities, $2k_a k_b/(k_a + k_b)$. Cleary and Monaghan report that this model accurately captures both transient and steady state temperature profiles for conductivity ratios, $k1/k2$, as high as 1000.

Using model E (eqn. 4.14) along with the harmonic mean of viscosities analogous to eqn. 4.19, the viscosity discontinuity may be modelled as

$$\langle \frac{1}{\rho} \nabla \cdot \tilde{\sigma} \rangle_a = \sum_b \frac{m_b}{\rho_a \rho_b} \frac{4 \mu_a \mu_b}{\mu_a + \mu_b} \frac{\mathbf{r}_{ab} \cdot \nabla W_{ab}}{r_{ab}^2} \mathbf{u}_{ab}. \tag{4.20}$$

4.5 Results: Testing the viscosity model

4.5.1 Couette Flow

For these tests a small domain of height = 1 unit and width = 0.4 unit is set up with 160 fluid particles. The domain in periodic in x-direction with no-slip walls at the top and bottom. The fluid interface is at $y = 0.5$ unit.

Reynolds number variation

Viscosity of the lower fluid, ν_{lower} is fixed at 0.01, and the upper fluid is 10 times more viscous. Figure 4.1 shows the velocity profiles for different Re (UH/ν_{low}) values at simulation time, $t = 100$ unit. The timestep values used were $\Delta t = 5 \times 10^{-4}$ unit for $Re < 20$ and $\Delta t = 10^{-4}$ for $Re > 20$. The Reynolds number is varied from 0.1 to 1000.

No-slip condition at both walls is being met accurately. A very good agreement with analytical velocity profiles is observed upto $Re = 100$ after which there is deviation from the analytical profile. This is due to particle disorder and eventual breaking-up of the interface at higher Re values. The mixed and unmixed particle distributions are shown in figure 4.2b and figure 4.2a respectively. Stratified Couette flow has been shown to be unstable in a wide range of paramaters [27]. Moreover, the growth rate of the instability is proportional to Re [28]. So, it is expected that for higher Re values perturbations of the interface will grow causing eventual interface break-up and mixing of fluid particles.

It can be seen from figure 4.1d that at $Re = 1000$ the extent of mixing is such that the entire fluid is seen to behave as a single phase.

Viscosity ratio variation

In this test Re (UH/ν_{higher}) is held constant at 0.0125 and the viscosity ratio is allowed to vary. Figure 4.3 shows the velocity profiles for different viscosity ratio (m) values at simulation time, $t = 100$ unit. The timestep values used were $\Delta t = 5 \times 10^{-4}$.

We see a very good agreement with analytical results for m values as high as 300. At higher values of m we observe tensile instability in the phase with higher viscosity.

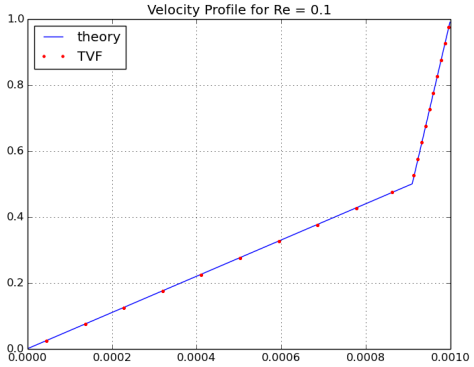

(a) Re=0.1

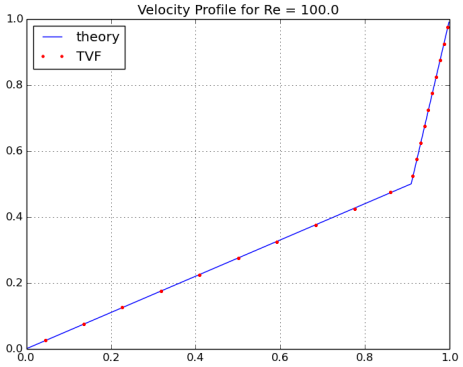

(b) Re=100

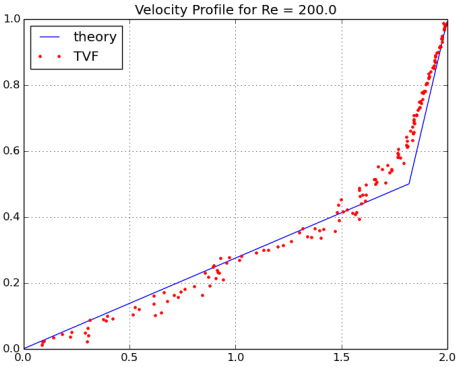

(c) Re=200

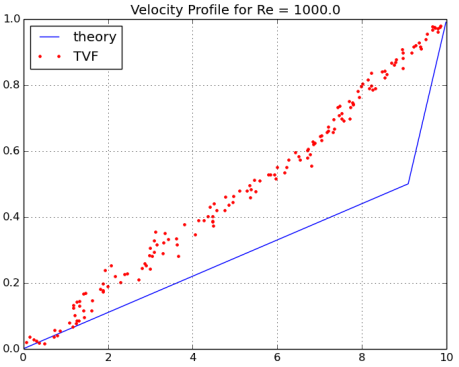

(d) Re=1000

Figure 4.1: Comparison of velocity profiles in strafied Couette flow for different Re at $t = 100$; viscosity ratio = 10

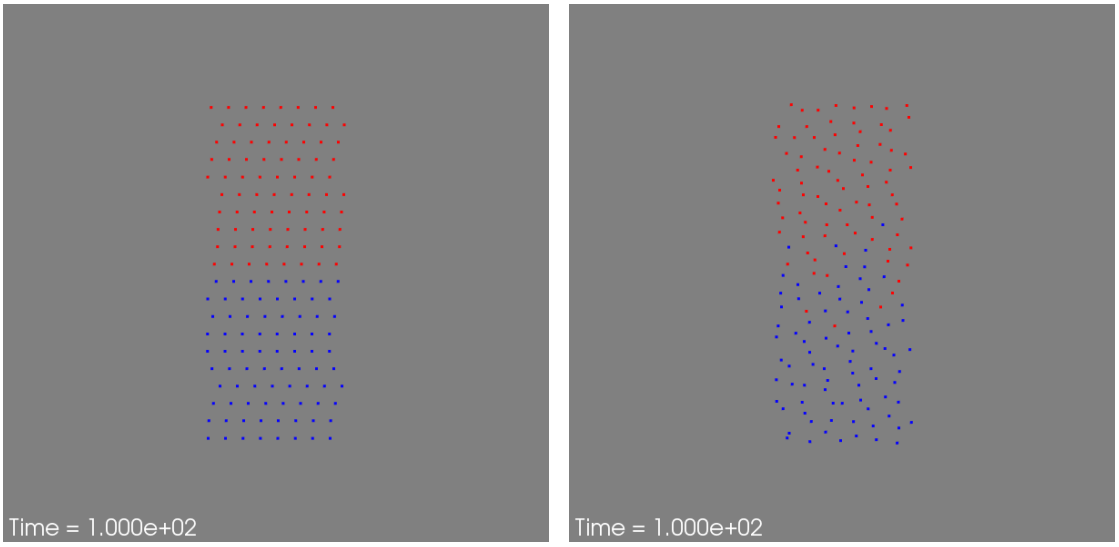

(a) Unmixed ($Re = 1$; $m = 10$; t=100) (b) Mixed ($Re = 200$; $m = 10$; t=100)

Figure 4.2: Particle distribution in Couette Flow

Particles collapse into tightly stuck pairs as shown by red particles in figure 4.4. This instability is explained in Appendix C.

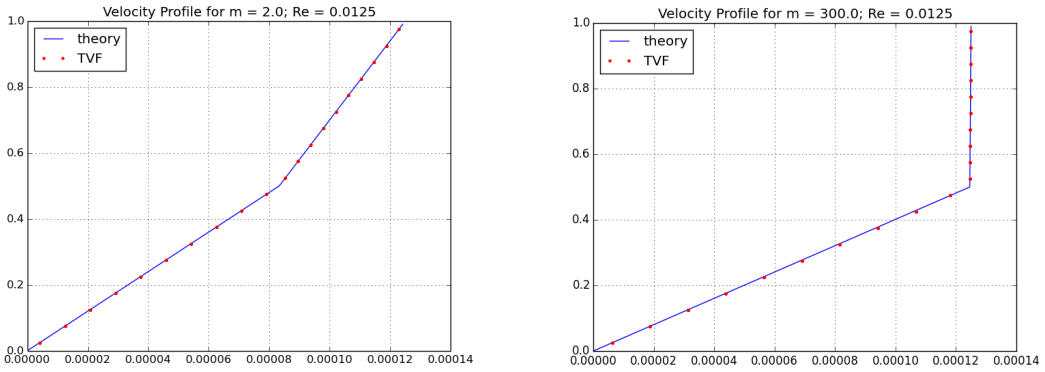

(a) $m = 2$ (b) $m = 300$

Figure 4.3: Comparison of velocity profiles in strafied Couette flow for different viscosity ratios at $t = 100$; $Re = 10$

Therefore, the model gives very good results for a range of Re and viscosity ratios as long as the particles do not mix-up or are prone to other SPH instabilities.

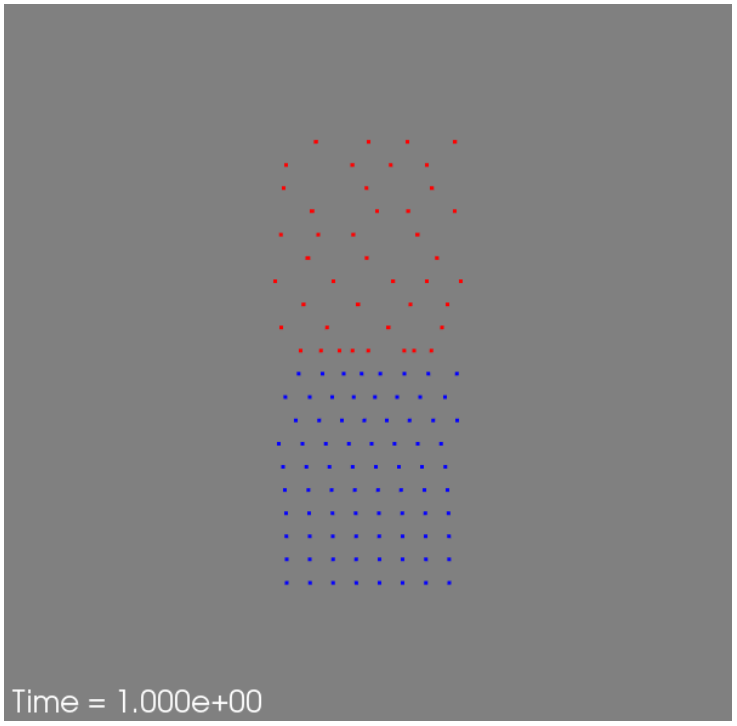

Figure 4.4: Tensile instability in phase with higher viscosity; Couette flow, m=400, Re=0.0125

4.5.2 Poiseuille Flow

For these tests a small domain of height = 1 unit and width = 0.4 unit is set up with 4000 fluid particles. The domain in periodic in x-direction with no-slip walls at the top and bottom. The fluid interface is at $y = 0.5$ unit.

Viscosity of the upper fluid, ν_{up}, is 0.01, and the lower fluid is 10 times more viscous. Figure 4.1 shows the velocity profiles for different Re values at simulation time, $t = 100$ unit. In this case Re is defined using the mean flow rate as the velocity scale, channel height as the length scale and the viscosity of the upper fluid, ν_{up} as the kinematic viscosity. Therefore the Reynolds number is given by

$$Re = \left(\frac{gH^2}{96\nu_{up}} \frac{m^2 + 14m + 1}{m(m+1)} \right) \frac{H}{\nu_{up}}, \tag{4.21}$$

where g is an external acceleration applied to the fluid in the x direction which acts as the driving pressure gradient. Re is varied from 1 to 1000, timestep values used were $\Delta t = 7.5 \times 10^{-5}$ unit.

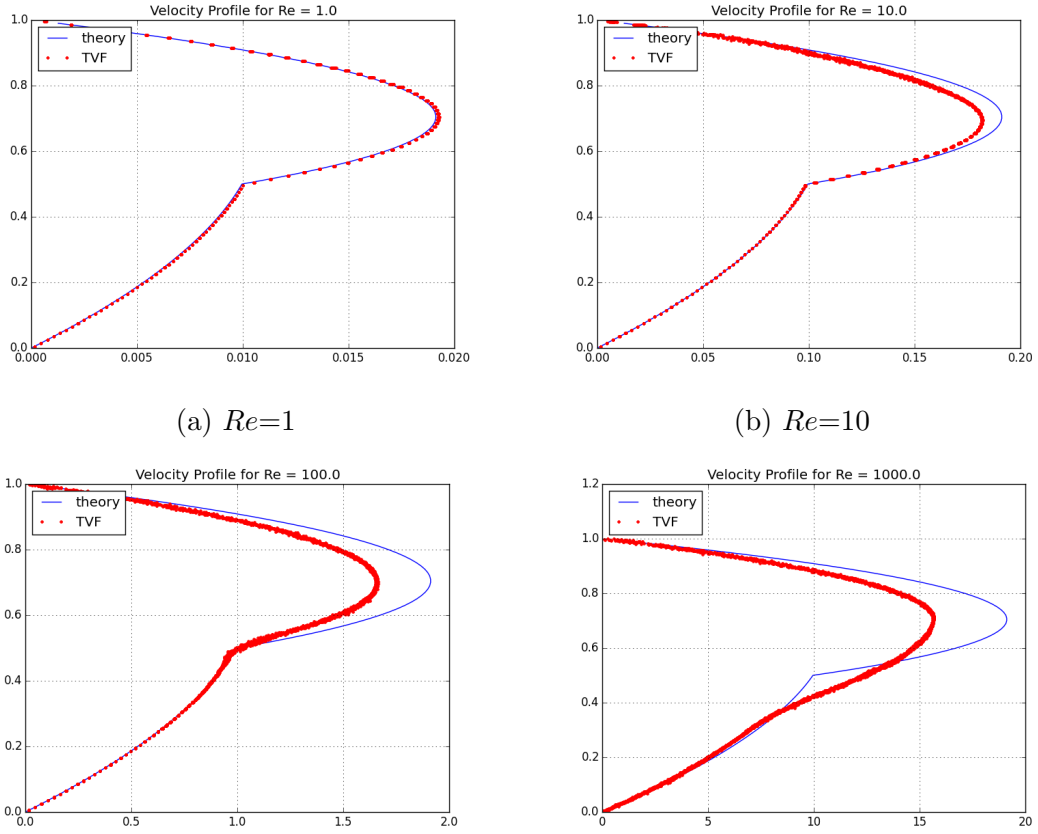

(a) Re=1 (b) Re=10

(c) Re=100 (d) Re=1000

Figure 4.5: Comparison of velocity profiles in strafied Poiseuille flow for different Re at $t = 100$; viscosity ratio = 10

Figure 4.5 shows a good agreement in the numerical and analytical results for $Re = 1$. As Re increases the numerical profile deviates from the analytical profile. The reason for this is the same as in Couette flow. At higher Re values particle disorder sets in faster. Moreover, stratified Poiseuille flow is unstable under a wide range of parameters [27]. Higher Re cases are more unstable than low Re cases. The instability causes growth of disturbances at the interface, and eventual mixing of phases. Figure 4.6 shows the particle distributions at $t = 100$ unit.

Note that the sound speed is held constant at 20 for all the tests mentioned in section 4.5. In order that variations in the density be lower than 1% the sound speed set in the simulations must be at least 10 times the velocity scale [8]. Therefore, for cases with $Re > 100$, this condition is not met and there is significant deviation from the incompressibility condition.

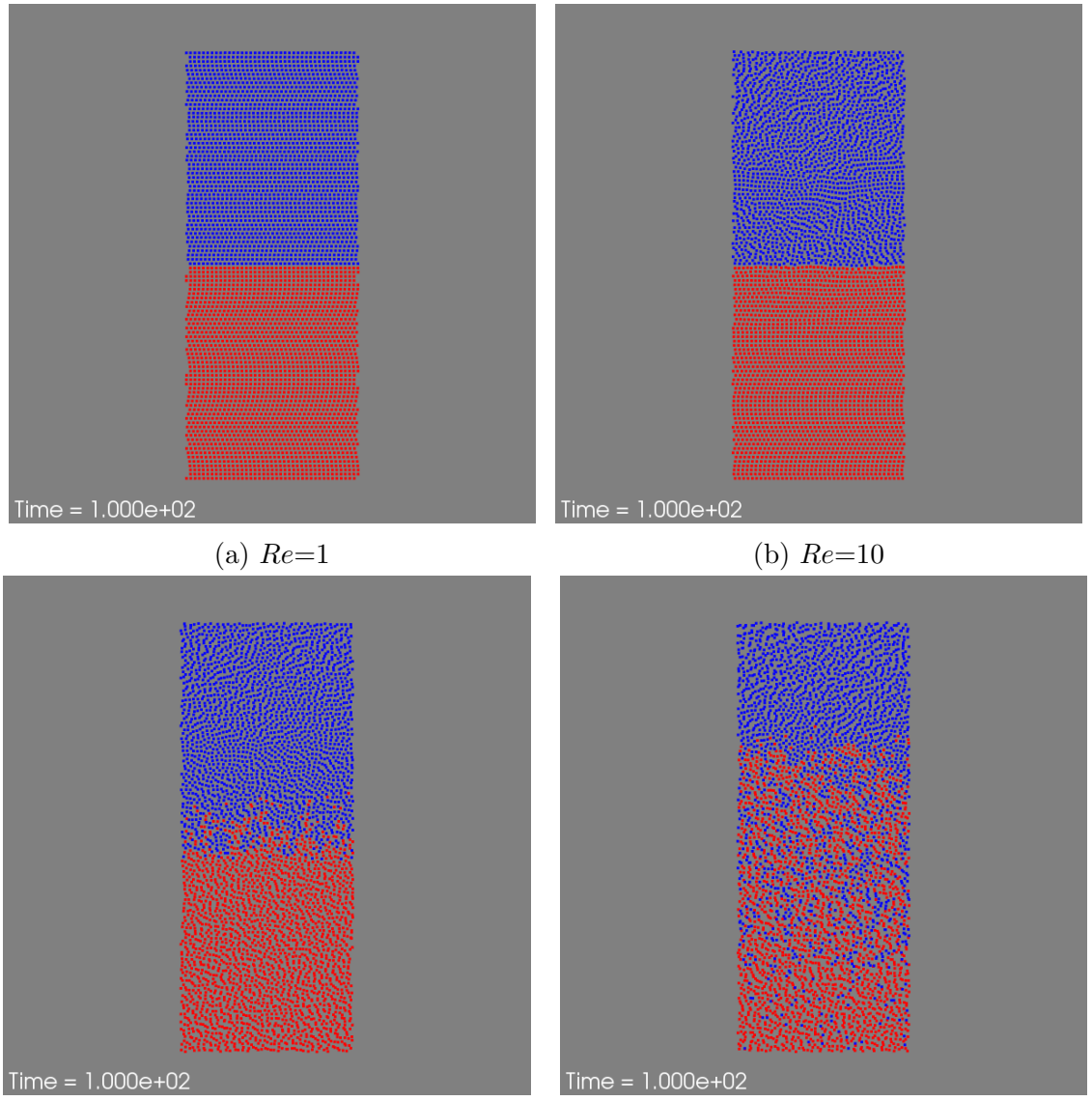

(a) Re=1 (b) Re=10

(c) Re=100 (d) Re=1000

Figure 4.6: Comparison of velocity profiles in strafied Poiseuille flow for different Re at $t = 100$; viscosity ratio = 10

4.5.3 Comments

A clear problem with the stratified viscosity scheme devised in this thesis is that when particles near the discontinuity become disordered, the shear stress balance is violated and we start getting incorrect velocity fields.

Cleary and Monaghan [26] have developed the discontinuous conductivity model keeping solids in mind. In solid materials the SPH particles have little or no relative motion, and hence, no disordering. The tests conducted on disordered particles are limited to materials

with uniform conductivity.

The tests were conducted with flat or close to flat interfaces. The performance of the model in case of arbitrarily shaped interfaces has not been tested here or by Cleary and Monaghan [26]. In case of viscosity strafied flows we often have a jagged interface. Often, the regions where the interface is sharp are stretched to the point that thin offshoots of thicker fluid are observed in the thinner fluid (see figure 4.7). These are referred to as 'fingers'. It is not clear how well the model will hold in such cases.

The model is able to handle a wide range of Reynolds numbers and viscosity ratios as long as the phases do not mix.

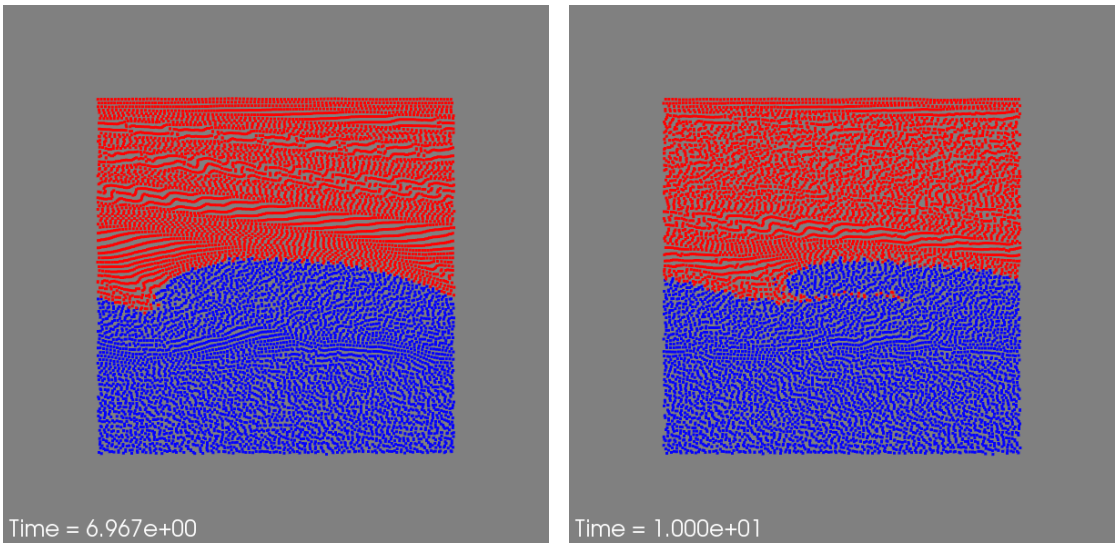

Figure 4.7: Evolution of interface in viscosity stratified flow

Chapter 5

Initial Perturbation

Accurately initialising the problem is of utmost importance in stability problems. The base flow may be compared to an 'unstable equilibrium' in a rigid body system. It means that any small deviation from the stable state grows and the system does not return to the stable state.

In the absence of any initial perturbations, the fully developed base flow in case of KHI or viscosity stratified flows would remain unaffected in time but due to perturbations, the system becomes unstable almost immediately.

These systems are very sensitive to the nature of the perturbation. In order to validate the numerical method, we must carefully introduce a perturbation which is consistent with the governing equations for the flow and more specifically with the solution we are validating it against.

5.1 Initialisations in literature

In all the numerical studies of fluid instability the problem is set up using one of the following three methods.

5.1.1 Position Perturbation

This method has been used by Cao et al. [28] with a finite difference method. It was used by Shadloo et al. [5] [4] with SPH.

In this method, the interface is set along a sinusoid (with a low amplitude) at $t = 0$ as

$$y = A\sin[2\pi x/\lambda]. \tag{5.1}$$

There are two main problems with this method:

1. If the discretisation points are located on a uniform cartesian grid, then we have a jagged interface which means that we have unwillingly introduced higher frequencies in the interface.

2. While the interface has a non-zero pertubation, the velocity field is not perturbed which leads to inconsistency with governing equations.

Small Perturbation

Cao et al. [28] use the simple position perturbation to initialise a viscosity-stratification problem but with an extremely small perturbation amplitude (5×10^{-4} unit). They report that this initialisation gives exponential growth right from $t = 0$. Here we use the same initialisation with KHI and get exponential growth not exactly from $t = 0$ but from $t \approx 0.2$ (figure 5.1).

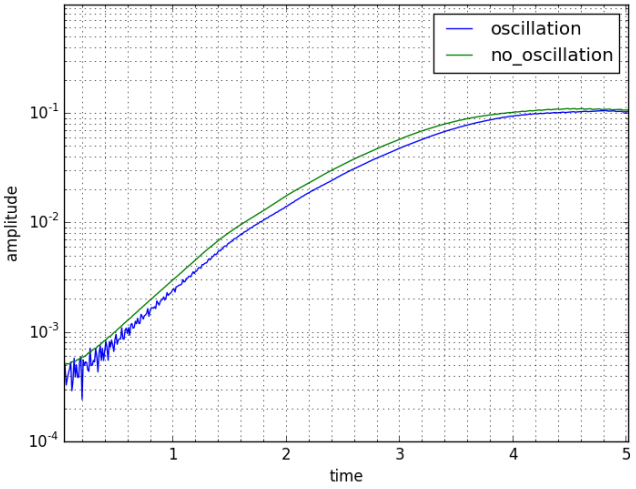

Figure 5.1: Low amplitude initialisation for KHI

An issue with this method is that at amplitudes as low as 5×10^{-4} unit, pressure oscillations due to the weakly-compressible nature of our scheme become prominent. In

order to get rid of the pressure waves at $t = 0$, a higher viscosity is used to arrive at the initial particle distribution. Then using this particle distribution the actual simulation is run.

5.1.2 Velocity Perturbation

In this method the interface is perfectly flat at $t = 0$ and is advected under a velocity field to trigger the instability. Price [3] and Agertz et al. [29] use a velocity field like

$$v_y = A \sin[2\pi x/\lambda], \tag{5.2}$$

which does not vary with y location. Read et al. [10] have used a y-velocity field which decays exponentially in magnitude away from the interface, such as

$$v_y = A \sin[2\pi x/\lambda] e^{-B(y-y_0)^2}. \tag{5.3}$$

The problem with such an initialisation is that it is not consistent with any linearised perturbation solutions.

5.1.3 Vortex Sheet

The interface for KHI may be modelled as a vortex sheet. Pullin [30] and Rangel et al. [31] [32] have used a vortex-sheet discretisation method. Here, the discrete vortices are placed on a curve like eqn. 5.1 at $t = 0$. This is a consistent way of doing the initialisation but care must be taken to place the vortices at a uniform distance from each other along the sine curve, i.e. the vortex sheet must not be stretched non-uniformly in the process of deforming the interface.

5.2 KHI Potential Flow Solution (linear regime)

Analytical growth rate for KHI is obtained by solving a linearised potential flow problem. The growth rate is sensitive to the initial conditions. In the linearised potential flow problem, when the interfacial perturbation is introduced the velocity potentials are also

perturbed. We are left with first order perturbation terms in the velocity field. These terms have a non-negligible effect on the growth.

Two inviscid fluids are considered flowing over each other in a domain with infinite depth and height. Kelvin's circulation theorem holds in this case. We assume that there is no rotational perturbation at the start, therefore, the fluids remain irrotational. The analysis is further restricted to incompressible flows, so that a velocity potential may be assumed in the two phases. The linear stability analysis is presented in Appendix A, here we derive only the velocity fields.

5.2.1 Velocity field at $t = 0$

The functions $\tilde{\phi}_1$ and $\tilde{\phi}_2$ represent the velocity potentials of the fluid on top and the fluid at the bottom respectively.

$$\tilde{\phi}_1 = U_1 x + \phi_1 \tag{5.4}$$

$$\tilde{\phi}_2 = U_2 x + \phi_2 \tag{5.5}$$

$$(\zeta, \phi_1, \phi_2) = (\hat{\zeta}, \hat{\phi}_1, \hat{\phi}_2) e^{ik(x-\omega t)} \tag{5.6}$$

we have a growing solution because $\omega_i > 0$ (considering unstable mode only). Gradients of the potential functions give us the respective velocity field in the two fluids. The final velocity field is given by

$$v_2 = -i(\omega - kU_2) e^{i(kx-\omega t)} \hat{\zeta} e^{-kz}, \tag{5.7}$$

$$v_1 = i(\omega - kU_1) e^{i(kx-\omega t)} \hat{\zeta} e^{kz}. \tag{5.8}$$

Here we present a simplified case where $-U_1 = U_2 = U$, $\rho_1 = \rho_2 = \rho$ and surface tension is absent. Unstable growth rate, ω, for this case is given by (Appendix A)

$$\omega = ikU. \tag{5.9}$$

Taking just the real parts we get

$$Re(v_2) = kU\hat{\zeta} e^{-kz} e^{kUt} (\cos(kx) - \sin(kx)), \tag{5.10}$$

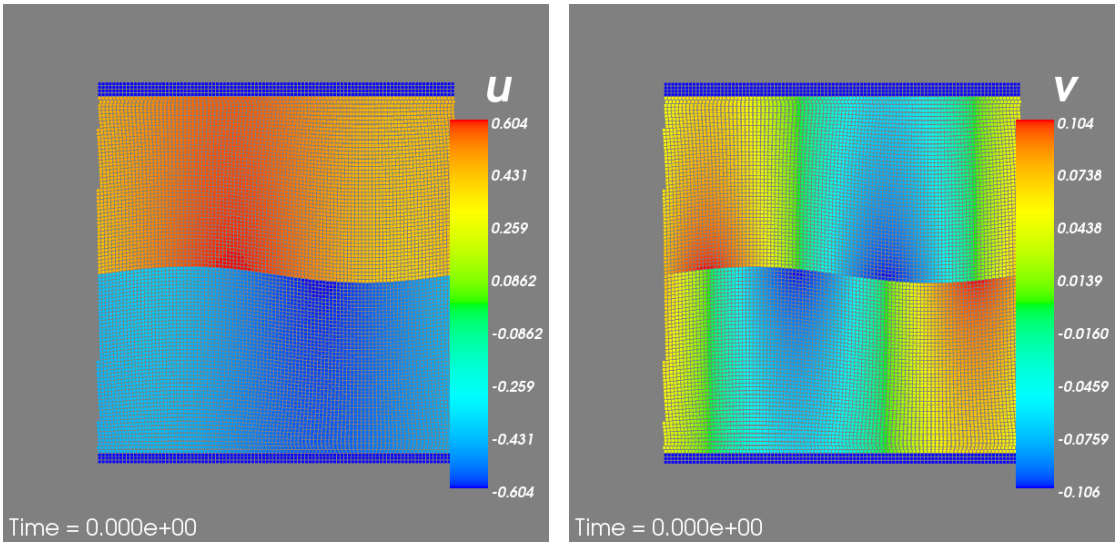

(a) u field (b) v field

Figure 5.2: Analytical velocity field at $t = 0$

and

$$Re(v_1) = -kU\hat{\zeta}e^{-kz}e^{kUt}(\cos(kx) + \sin(kx)). \tag{5.11}$$

Similarly for the u velocity we get

$$Re(u_2) = kU\hat{\zeta}e^{-kz}e^{kUt}\left(\cos(kx) + \sin(kx)\right), \tag{5.12}$$

and

$$Re(u_1) = kU\hat{\zeta}e^{-kz}e^{kUt}\left(\cos(kx) - \sin(kx)\right). \tag{5.13}$$

Fig 5.2 shows the u and v fields at $t = 0$.

5.3 Improved initial perturbation

As seen in section 5.1 there were two issues with the initialisations, namely:

1. Higher frequencies - reproducing any smooth curve on a uniform cartesian grid introduces higher frequencies

2. Inconsistent velocity field perturbation - the velocity field must be perturbed in accordance with the interface perturbation

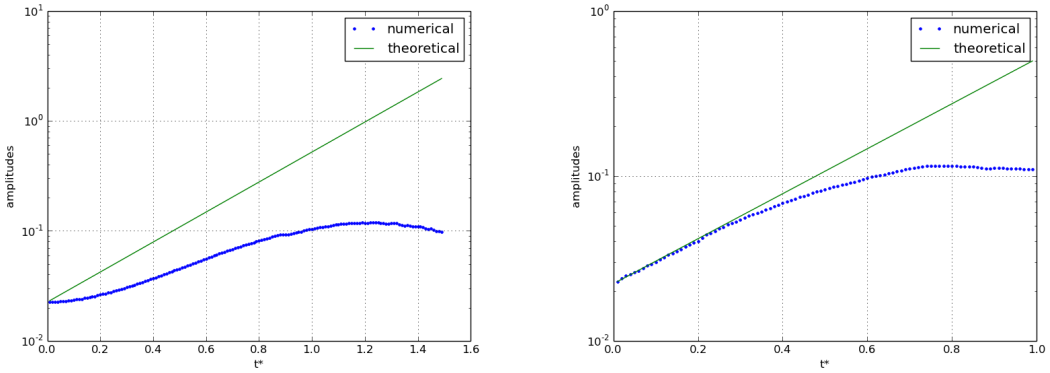

(a) Unperturbed **v** (b) Perturbed **v**

Figure 5.3: Difference of growth at $t = 0$

In order to eliminate the first issue we start the simulation with a particle distribution which ensures that the interface is smooth. To get such a particle distribution we begin with a flat interface and using a v-velocity field (no u-velocity), advect the interface till we have a suitable interface shape i.e. a sinusoid with a certain amplitude. The velocity field used is like those in subsection 5.1.2.

In order to eliminate the second problem we initialise the particles with velocities calculated analytically (sec 5.2). While that the analytically derived field is for an infinite, inviscid domain we get fairly accurate results when it is used for the simulation.

5.4 Comparison of the initialisations

We compare the evolution of the interface with improved initial perturbation (section 5.3) against the initialisation described in section 5.1.1. The most striking difference is seen in the growth rates.

Figure 5.3b shows the growth when we begin with a velocity field that includes the first order terms. Figure 5.3a shows the growth without the first order velocity terms. In figure 5.3a, it is clear that the growth rate at t=0 (slope of the curve) is 0. In this initialisation the interface has no v-velocity at t=0. The perturbation starts growing but the growth is not exponential (exponential growth would be seen as a straight line segment on the semilog plot). After some initial time, the perturbation becomes so high that the linear approximation fails and we cannot expect an exponential growth after this. In figure

5.3b we see that the amplitude starts increasing right from t=0, moreover, it is in close agreement with the theoretically obtained values. As the amplitude starts approaching 0.1, we start seeing deviation from the theoretical result as expected.

Note that the cases demonstrated here are viscous, with $Re = 1000$. The simulations are done in a periodic (x-direction) domain of height and width 1 unit with 100×100 particles. The wavelength is the same as the width. The base density, $\rho = 1000$ unit, the velocity difference between the two fluids, $\Delta U = 1$ unit. The sound speed is 10 times the characteristic velocity, ΔU, i.e. $c = 10$ unit to keep the density fluctuations less than 1% [8].

5.5 Forcing a perturbation

Initialising the KHI problem accurately was possible as the linearised perturbation solution to the problem was known. Solutions for other instability problems may not be available. Hence, we need an initialisation scheme which works uniformly for all cases.

Just perturbing the interface without perturbing the fluid velocity produces a fluid field with a finite divergence. The system takes some time to adjust itself to produce a divergence free velocity field.

We start with a perfectly flat interface, with no perturbation. Then, we perturb the interface using an external body force near the interface for a very short time. This will act like an actual external perturbation, putting the system in an unstable state. The forcing is given by

$$f_y = \sin\left(2\pi\frac{x}{\lambda}\right) e^{-y/H}. \tag{5.14}$$

5.5.1 Transient Region in Growth

This initialisation ensures that the velocity field is divergence free at all times, but it is not consistent with the theoretical analysis. There is an external body force being applied which obviously affects the growth rate.

The external force, although for applied for a short duration ($t^* \approx 0.01$ unit), changes the flow field. Even after application of this force is turned off, the velocity field generated

by this forcing remains. KHI takes a finite time to overcome the effect of this external forcing.

Instead of an exponential growth from $t = 0$, we see a linear growth near $t = 0$. This eventually tends to an exponential growth. This trend can be seen in the four plots of figure 5.4. We want this 'transient region' to be of a minimum duration, hence studying the factors that affect it becomes important. Figure 5.4 shows the effect of different flow parameters and numerical parameters on the length of this transient.

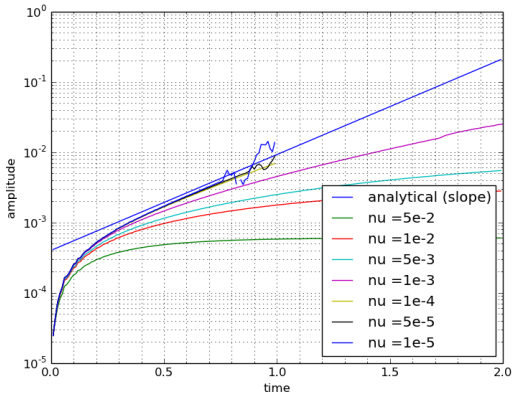

(a) Dependence on viscosity

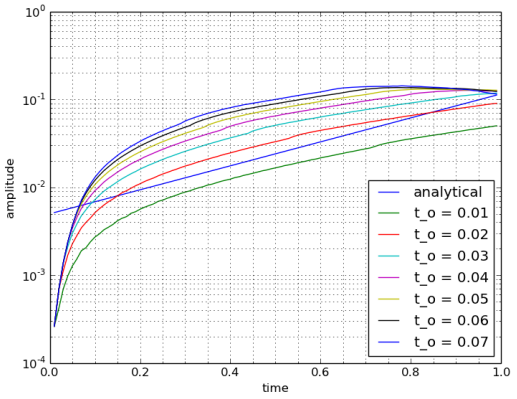

(b) Dependence on t_0

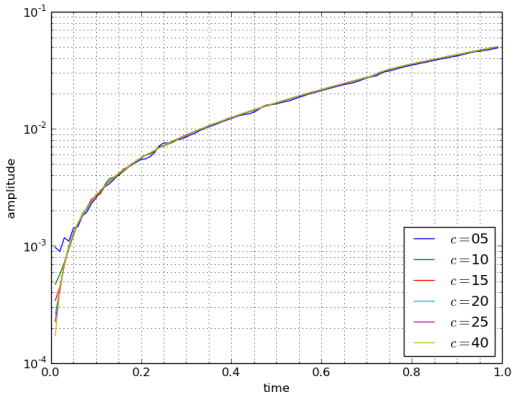

(c) Dependence on sound speed, c

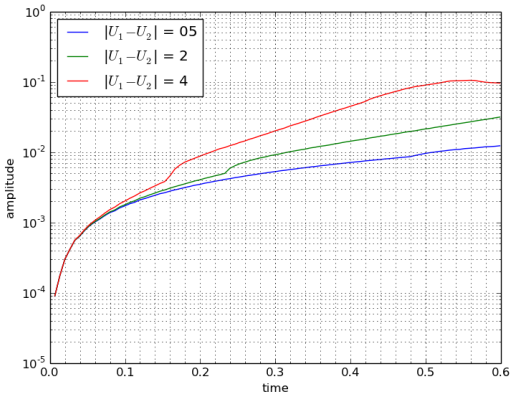

(d) Dependence on ΔU

Figure 5.4: Effect of various factors on transient

All the plots in figure 5.4 are on a semilog scale. The transient is said to vanish when the growth curves become straight lines, that is when the growth is exponential. The transient is probably due to all eigenmodes being activated by forcing instead of just the unstable ones. The transient represents time taken for the stable mode to decay.

Figure 5.4a compares the transient across a range of kinematic viscosity, ν, values. We

can see that at low values of viscosity the transient exists for a slightly longer duration. But the effect of viscosity seems negligible considering that it is varied by over 3 orders of magnitude to see any perceivable difference. In figure 5.4b we see the effect of the cutoff time, t_0, i.e. the amount of time for which we apply the external forcing, on the transient. Smaller t_0 values give better results because they perturb the interface to a lower amplitude to begin with, but the duration of the transient is unaffected by t_0. The third test is the dependence on the numerical sound speed, c, used for the simulations. Speed of sound affects how fast the pressure waves travel and how accurate the incompressibility is. Figure 5.4c shows that duration of transient is independent of c as well. Finally we tested the dependence on the characteristic velocity, ΔU, and figure 5.4d shows no dependence.

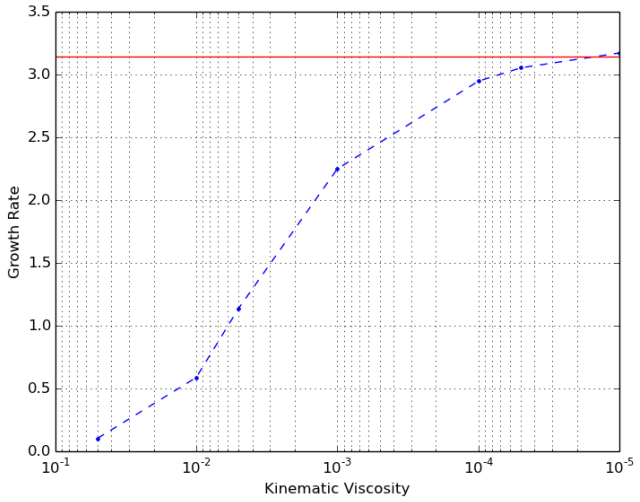

Figure 5.5: Growth rates converging to the analytical value as viscosity reduces

Figure 5.5 shows that the growth values converge to the analytical value as viscosity is reduced. This means that in all the cases we eventually get the exact growth rate the duration of the transient is unaffected by any of them.

5.6 Conclusions

Stability problems are sensitive to initial conditions. Perturbing either the interface or the velocity fields independent of each other may lead to an unphysical velocity field with a non-zero divergence value. It also leads to incorrect growth rates. Starting with a very

small initial perturbation reduces the inconsistency, but is prone to noise.

While using the exact initialisation gives accurate results, it is not always possible. For most problems analytical expressions for velocity fields are not available. Hence, we need a general method for initialising the problems.

Forcing the interface externally can lead to correct growth rates, but it requires very small initial amplitudes or initial transient dominates.

Chapter 6

Results & Conclusions

Growth rates of instabilities in the liner growth regime have been used for validation. Here, we begin with an explanation about how the measurement of growth rates is done and then present results for the two broad cases considered: KHI (velocity discontinuity), and viscosity-stratification (shear discontinuity).

6.1 Growth Rate Calculation

The only analytical solutions possible for the cases being studied exist for small time periods. Growth rate near the start ($t = 0$) is used for validation of code.

The interface is being captured by advection of the colour field. If fluid particles of different phases are assigned colours c_1 and c_2, the interface is characterised by the colour contour with value $(c_1 + c_2)/2$. The interface may be a linear combination of several wavelengths. Analytical solutions give us the growth rate associated with each wavelength.

In the numerical simulations, a single wavelength perturbation is inserted at $t = 0$, the interface is allowed to evolve and the growth of this wavelength is tracked with time. Following is a description of three methods which may be used for capturing growth.

6.1.1 Simple Crest-Trough

In all of literature the amplitude of perturbations is simply obtained by taking the difference of position of the crest and trough perpendicular to the wave. This may be erroneous due to two reasons:

- Errors in peak values are directly translated to amplitude

  - The maximum and the minimum values of the interface y-location are tracked, the amplitude is obtained from just these two points

  - Information from the rest of the points is ignored

  - Errors e_1, e_2 in the two values are scaled only by a factor of 2

- Presence of other wavelengths

  - The method inherently assumes that there is only a single wavelength present

  - In case there are multiple wavelengths present it fails to capture specifically the wave of interest

Further, y-coordinates of the particles themselves should not be used as crest and trough y-coordinates. This is incorrect because the particles themselves do not represent the interface.

6.1.2 Diffused Interface

In this method we fit a curve through the interface-band. In section 3.2.1 we have described a surface dirac delta function, δ_s, which is used in the CSF implementation of surface tension. The value of this function is highest near the fluid-fluid interface and decays sharply away from it. δ_s is used for characterizing the interface.

We identify a 'band' of particles which satisfy $\delta_s > \delta_0$, where δ_0 is an appropriately chosen cutoff value. In this study the typically used value is $\delta_0 = 0.26/h$, where h is the kernel smoothing length used in the simulation. This value for δ_0 is chosen such that the region identified as the interfacial region is thin ($< 4\Delta x$). The magnitude of δ_s is directly related to the smoothing length of the kernel. The colour field has a sharp gradient at the interface, the SPH approximation of this gradient is directly dependent on the smoothing

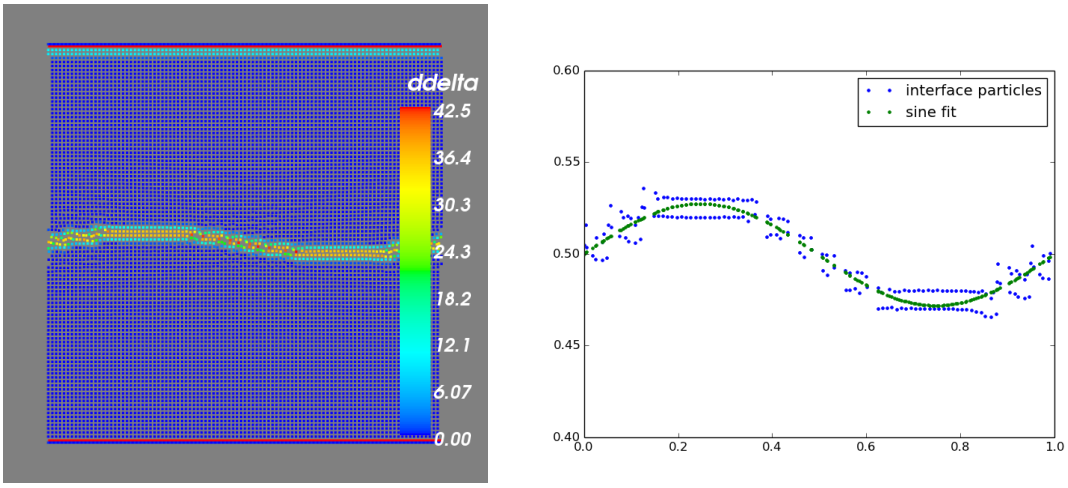

(a) δ_s over the domain (b) The sinusoidal fit in the interface band

Figure 6.1: Capturing the interface: Diffused

length, h. The gradient values are high for low values of h, and low for high values of h i.e. δ_s is inversely related to h, and the choice of δ_0 must be made accordingly.

Now, to obtain the amplitude of perturbation we fit a sinusoidal curve through this scatter of points. A least-squares fitting is done where the amplitude and phase of the sine curve are allowed to vary while holding the wavelength constant. The amplitude is unknown and it varies with time. As the fluid flows the wave may propagate with respect to the walls, hence the phase is also allowed to vary.

Problems with this method:

- δ_0 is an arbitrarily chosen number which affects the thickness of the band.
- As the simulation evolves, particles enter and leave this band ($\delta_s > \delta_0$). This sudden appearance or disappearance of points in the scatter manifests as a sharp change in the growth trend.

6.1.3 Undiffused Interface

In this method the actual interface characterised by the $(c_1 + c_2)/2$ contour is being tracked. This is a three step process:

1. Colour field is interpolated onto a Cartesian grid. Figure 6.2a shows the interpolated colour field.

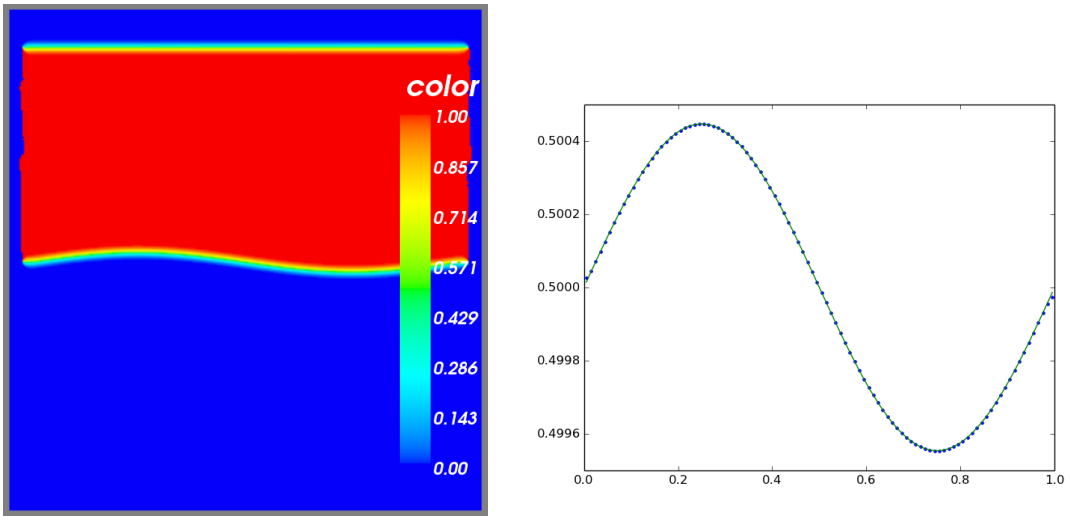

(a) Inerpolated colour field (b) Curve fit through interface

Figure 6.2: Capturing the interface: undiffused

2. At each x-location on the grid, we obtain the $(c_1+c_2)/2$ point via a linear interpolation in y-direction - this gives interface coordinates at uniformly spaced x-locations. In figure 6.2b the blue dots represent the y-locations obtained.

3. Amplitude of the wave of interest is obtained by a least-squares sine fit (as described in subsection 6.1.2) or by fourier analysis of this series. In figure 6.2b the green curve represents the sine fitting through the points.

Possible issues with this method:

- Close to the boundaries, interpolation under-predicts the function values. This issue has been elaborated upon in section 4.3. This is evident in the gradient observed near the top wall (no gradient is observed near the bottom wall as the color function for the lower fluid is set as 0). However, this has no effect on the interface capturing.

- SPH interpolation at each timestep is computationally expensive.

While initialising the problem, perfect periodicity must be ensured at the boundaries. Y-values obtained near the edge of the periodic boundaries are erroneous at times due to incorrect initialisation. In figure 6.2b it can be seen that the first and the last points deviate from the curve. This deviation can have a high magnitude and may affect the amplitude of the fitted curve. We ignored the last 2 particles on each side while doing the curve fitting to avoid this problem.

In this work the undiffused interface capturing method has been employed.

6.2 KHI

The instability of the interface between two parallel streams of fluid with different velocities is known as Kelvin–Helmholtz instability. KHI is a classic problem, it was first studied by Helmholtz and Lord Kelvin around 1870. For inviscid flows, in the absence of gravity and interfacial surface tension, any perturbation on such an interface will grow, forming what are known as billows, which ultimately leads to fluid mixing. The name KHI is also used to describe the more general situation of instability in a single phase flow with a velocity gradient. KHI is a commonly seen phenomenon in stratified geophysical flows like currents within the ocean or flow of different layers of the atmosphere over each other.

In most of the typical scenarios there is a density discontinuity at the interface with the denser fluid at the bottom. KHI essentially converts the kinetic energy of the fluid to potential energy. Thus, gravity and surface tension can be seen as stabilizing forces while inertia is the destabilizing agent. A linear stability analysis of KHI has been presented in Appendix A.

6.2.1 Reproducing Shadloo et al.

Shadloo et al. [5] [4] [6] use SPH for solving inviscid KHI. A Standard SPH (non TVF) formulation is used along with a simple CSF based surface tension scheme. We reproduced their work and found problems in the initialisation, the 'artificial viscosity' and in the way they measure the growth rates.

The density ratio for all these is kept constant at $\rho_2/\rho_1 = 2$ where $\rho_1 = 1000$ unit. $\approx 10^4$ fluid particles are used with $\Delta t = 10^{-5}$. Ri is varied only by changing the σ value, everything else is constant. A simple interface perturbation is used for the initialisation which gives growth rate equal to 0 at $t = 0$. But in this work an approximation has been made which gives an expression for the growth rate, G_n, as

$$G_n = \frac{\zeta/\zeta_0 - 1}{t^*}, \tag{6.1}$$

where ζ is the perturbation amplitude and t^* value is taken when the perturbation reaches 10% of the domain height ($\zeta = 0.1H$). It is an odd approximation considering that this point is well past the validity region of the linear stability analysis. Nonetheless, it gives surprisingly accurate results. In fig. 6.3, the slopes of theoretical curve and the approximated curve at $t^* = 0$ give the respective growth rates, they are in close agreement. Similarly, growth rates were calculated for several values of Ri as shown in figure 6.4. It

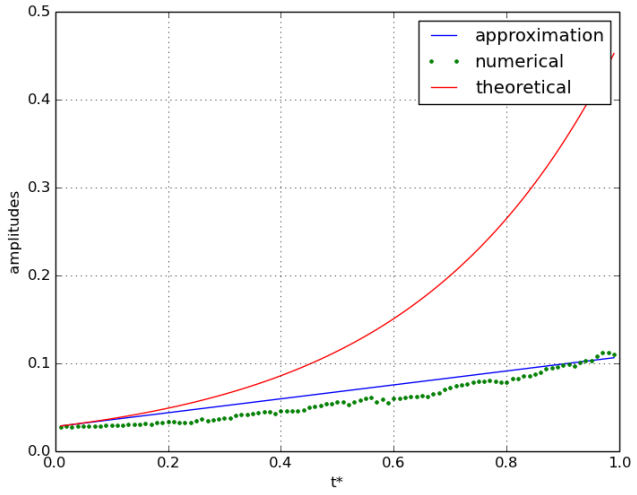

Figure 6.3: Analytical growth, numerical growth and the approximation used for getting the numerical growth rate

is seen that the analytical curve drops to zero at $Ri = 1$ which marks the cutoff point for the instability. We can see a close agreement between the analytical and numerical values in figure 6.4.

Shadloo et al. claim to use an artificial viscosity for the simulation but they actually use a model D (subsection 4.2.3) type viscosity, with a viscosity value equal to $\nu = 10^{-4}$. They report that on increasing the value of 'artificial viscosity' they get lower and lower growth rates. Shadloo et al. report that for lower viscosity values they get unstable simulations, which most probably means that they get a high amount of mixing at the interface.

The most glaring problem with this is the measurement of the growth rate (figure 6.3). We attempted to resolve the problem of incorrect initialisation and growth rate measurement.

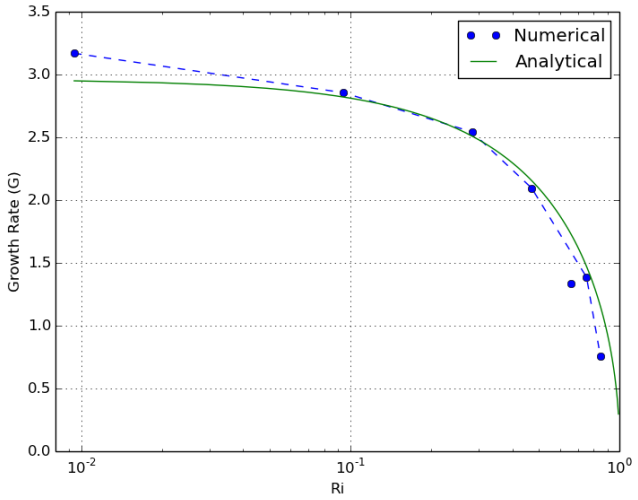

Figure 6.4: Comparison of the theoretical and numerical growth rates for $\rho_2/\rho_1 = 2$ for various Richardson numbers

6.2.2 Problem Setup

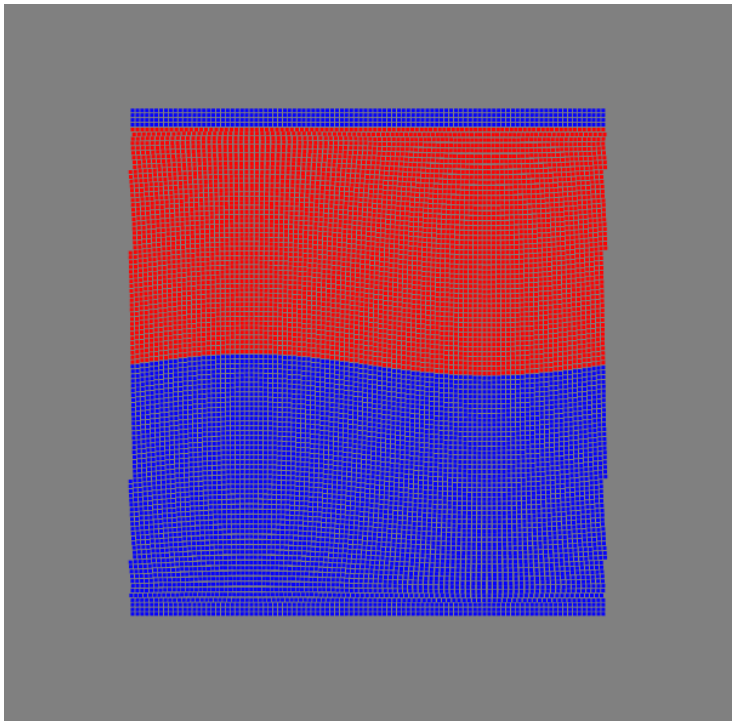

Figure 6.5: KHI problem setup

The problem is as defined in subsection 2.1.1. The same is shown in here in figure 6.5. The different coloured particles represent the two fluids flowing in opposite directions

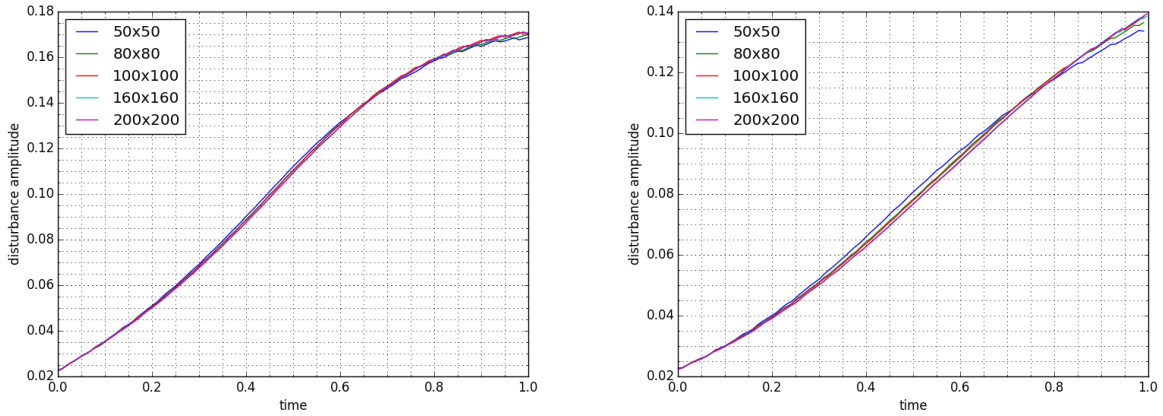

(a) Without surface tension

(b) With surface tension

Figure 6.6: Growth plots highlighting grid convergence

over each other. They are bounded by two solid walls moving at the same velocity as the base velocity of the fluid in contact. The domain is periodic in the x direction (direction of flow) in order to recreate an infinite domain. There is a sinusoidal perturbation of the interface and correspondingly there is a perturbation in the velocity field to begin with (see chapter 5).

The fluid velocities used in all the simulations are $U_1 = -U_2 = U = 0.5$ unit where U_1, and U_2 are x-direction velocities of the top and bottom fluids respectively. Speed of sound, c, is 20 unit. Density of the two fluid phases is equal to 1000 unit unless specified otherwise. In order to have the desired density, the mass, m, of each fluid particle is set as $m = \rho(\Delta x)^2$. The fluid domain (1x1 unit^2) is filled with 100x100 particles. The bottom wall has 3 layers, i.e. 300 particles and the top wall has 4 layers, i.e. 400 particles (the fourth layer is redundant and may be done away with). The same particle resolution is used in all simulations unless otherwise mentioned.

A quintic spline SPH kernel [24] is used in all the simulations with smoothing length, $h = 1.3\Delta x$. Interpolation using a quintic spline kernel involves particles interacting with other particles in a range of $r < 3h$. This means that during interpolation and hence while obtaining inter-particle forces each particle interacts with 48 particles on an average.

6.2.3 Grid Dependence

To check for dependence on the solution on the number of discretisation particles used we compared solutions of five cases (around 100×100) with different number of fluid particles. Figure 6.6 shows two cases, figure 6.6a shows growths in the absence of surface tension force and figure 6.6b shows growths in the presence of surface tension. The study is conducted for 50×50, 80×80, 100×100, 160×160 and 200×200 fluid particles. Only the particle spacing, Δx, is changed while holding everything else the same. The number of solid particles scales linearly with the number of fluid particles.

Surface tension forces are obtained from the curvature. The scale of the curvatures that can be captured is given by $\kappa_{max} = \pi/h$ [15] [16]. The expected curvature values are well within this limit even with a sparse grid. Nonetheless, a grid dependence test was conducted to confirm that the growth is not significantly affected by noise in curvature values arising out of a jagged interface.

Figure 6.6 shows the amplitude of the interfacial sine wave against time. For the case without surface tension (figure 6.6a) the curves are almost identical. For the case with surface tension (figure 6.6b) the curve representing 50×50 fluid particles is slightly off the other curves, the curves representing higher number of particles are almost identical.

It can be concluded from figure 6.6 that the solution is independent of the number of particles if more than 80×80 particles are used for a 1x1 unit^2 domain.

6.2.4 Mixing of fluids

Linear stability analysis of KHI tells us that the growth of the smallest wavelengths is the fastest. Small wavelengths, i.e. the higher frequency disturbances of the interface are therefore expected to grow fast. Discretising the interface introduces a high frequency noise on the interface. By doing a smooth interface initialisation this noise may be reduced.

Growth of the small wavelengths is visible as rapid velocity fluctuations near the interface. These fluctuations cause rapid disordering and mixing of fluid particles near the interface.

The presence of surface tension is expected to ensure that the phases remain immiscible. Surface tension forces are higher for higher curvatures (i.e. small wavelengths), and one

may expect them to be a perfect counter force for the KHI induced mixing. However, surface tension is not enough to enforce immiscibility in the simulations. A similar result has been reported by Pullin [30]. Pullin has used a vortex sheet model for studying KHI and Rayleigh–Taylor instability. He has reported that surface tension smoothes the irregularities but only for finite times after which the vortex sheet intersects itself signifying breakdown of the scheme, and in our case mixing of the phases.

Once particles of one phase enter the other phase, the normal and curvature calculations for the mixed particles produce incorrect values and we get incorrect surface tension forces on the particles. Hence, onset of mixing needs to be avoided.

Growth of the small wavelengths is observed as a high frequency noise in the velocity field near the interface. An ad-hoc way of solving the problem would be to smooth out the velocity field, a physical way of doing the same would be to introduce viscosity in the fluid. Although, introduction of viscosity is expected to damp out the growth of smaller wavelengths more, it will affect the growth of the large wavelength as well.

6.2.5 Dependence on Viscosity

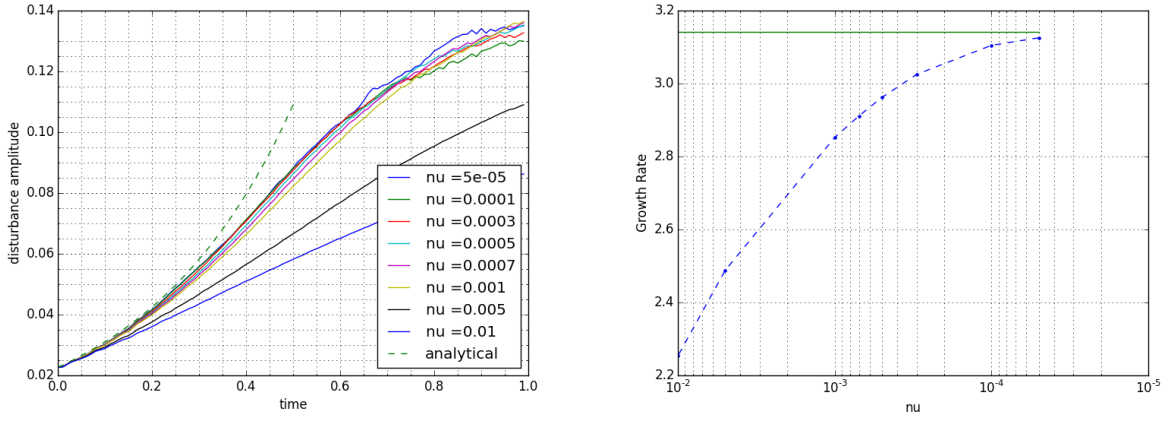

(a) (b)

Figure 6.7: Effect of viscosity on KHI growth

The analytical expression growth (see Appendix B) is derived for instability in inviscid fluids. The interface in inviscid fluids breaks up and the fluids mix as described in subsection 6.2.4. In the presence of viscosity mixing is substantially reduced.

We checked the dependence of growth on the amount of viscosity used. Viscosity based on model E (see section 4.2) has been used with kinematic viscosity, ν, varying between 10^{-2} and 5×10^{-5}. Figure 6.7, shows the results obtained. The dotted line in figure 6.7a shows the expected growth for an inviscid system and the solid lines show the growth obtained for different ν values. We see that for viscosities higher than $\nu = 10^{-3}$, the curves do not match. For lower viscosities, the curves are close to each other and to the analytical curve. In figure 6.7b the actual growth rate values are shown. The green line shows the analytically expected rate. It can be observed that as the viscosity reduces the growth rate converges to the expected value.

For obtaining the growth rates, an exponential function was fitted in the curves (upto $t = 0.5$) shown in figure 6.7a.

Viscosity values cannot be reduced to arbitrarily low values. In figure 6.7a we see that for the low viscosity cases the curves become jagged at higher times. The jaggedness is due to mixing of the phases. The mixing is more pronounced in lower viscosities, as was originially expected. Therefore, due to a trade-off between accuracy and particle mixing we have picked a value of $\nu = 5 \times 10^{-4}$ for our simulations.

6.2.6 Dependence on Surface Tension (Ri), Density Ratio

As mentioned earlier, surface tension and gravity are important stabilising forces for KHI. In this section we test the model in its ability to capture these phenomena.

We run a set of 3 cases, each set has a fixed ρ_2/ρ_1 value. We run each set with surface tension constant, σ, varying between 0 and 70 unit. For each case, the unstable eigenvalue for ω is evaluated (see Appendix A) as

$$\omega = \frac{2\pi\sqrt{\rho_1\rho_2}}{\rho_1 + \rho_2}|U_1 - U_2|\sqrt{1 - Ri}, \tag{6.2}$$

where the 'Richardson Number', Ri, is defined as

$$Ri = \frac{\rho_1 + \rho_2}{k\rho_1\rho_2(U_1 - U_2)^2}\left(g(\rho_2 - \rho_1) + k^2\sigma\right). \tag{6.3}$$

This ω is used to initialize the problem with the correct velocity field (see section 5.3).

Figures 6.8a, 6.9a and 6.10a show the growth of perturbation with time for the sets ρ_2/ρ_1 equal to $1, 2$ and 5 respectively. The different curves in the plots signify different values of the surface tension constant. Timestep values for all the simulations are $\Delta t = 10^{-5}$ unit. Figures 6.8b, 6.9b and 6.10b show the rate of growth value obtained by fitting an exponential curve through the data. The rates are plotted against Ri.

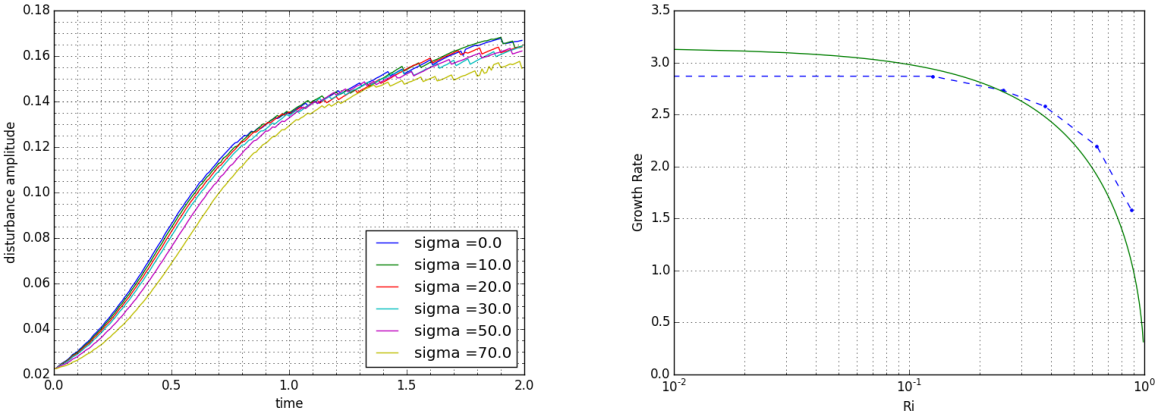

(a) (b)

Figure 6.8: KHI growth for $\rho_2/\rho_1 = 1$

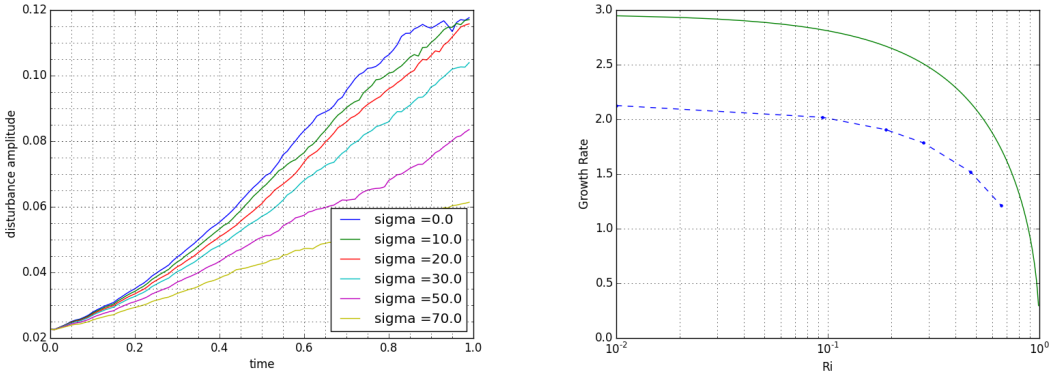

(a) (b)

Figure 6.9: KHI growth for $\rho_2/\rho_1 = 2$

While figure 6.8 shows a reasonable agreement between the numerical and analytical values, figures 6.9 and 6.10 show higher and higher deviation from analytical. This again is attributed mainly to fluid mixing.

Figure 6.11 shows evolution of the interface for $\rho_1/\rho_2 = 1$, $\sigma = 0$. By $t = 3$ we see a perfectly formed 'Cat's eye' vortex. For $\rho_1/\rho_2 = 2$ and 5 (figures 6.12, 6.13 respectively),

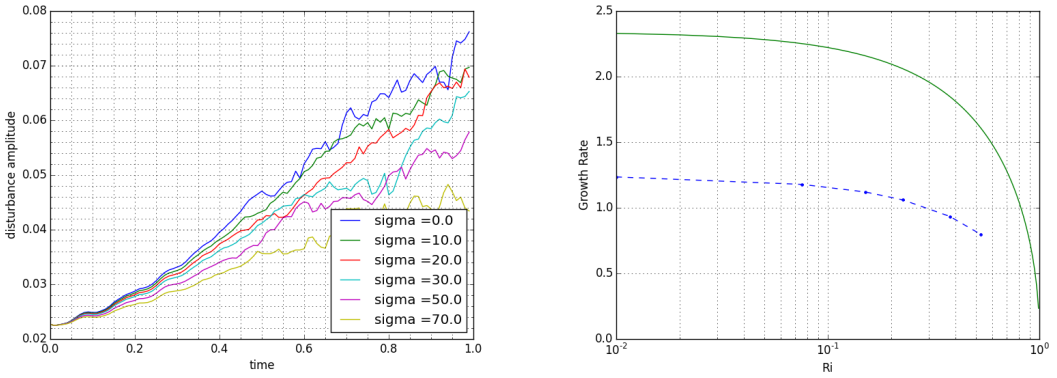

(a) (b)

Figure 6.10: KHI growth for $\rho_2/\rho_1 = 5$

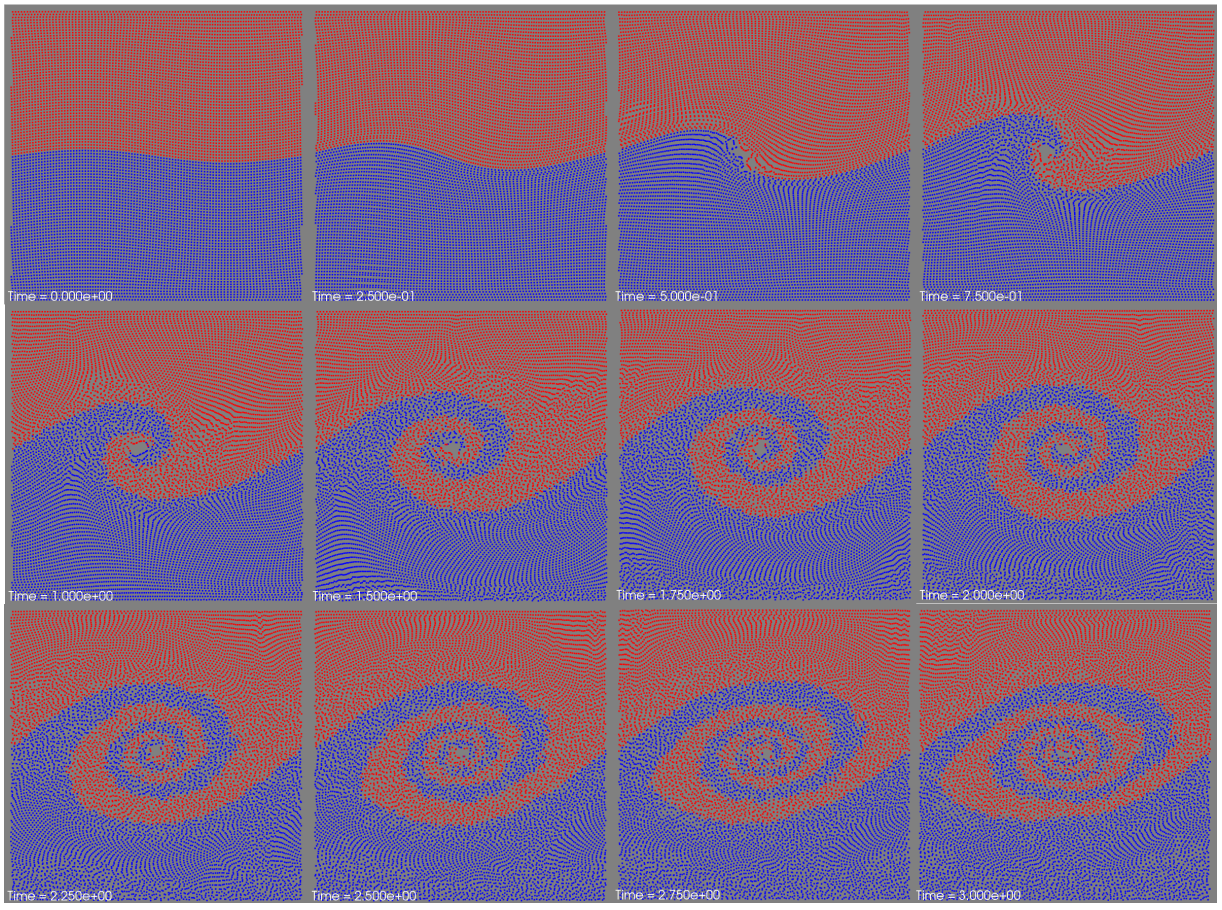

Figure 6.11: KHI interface evolution for $\rho_1/\rho_2 = 1$, $\sigma = 0$. Each frame is after a delay of $\Delta t = 0.25$

we do not get such a clean vortex as the phases start mixing at the interface much before that.

We saw that viscosity was important for ensuring that the fluids do not mix. Here,

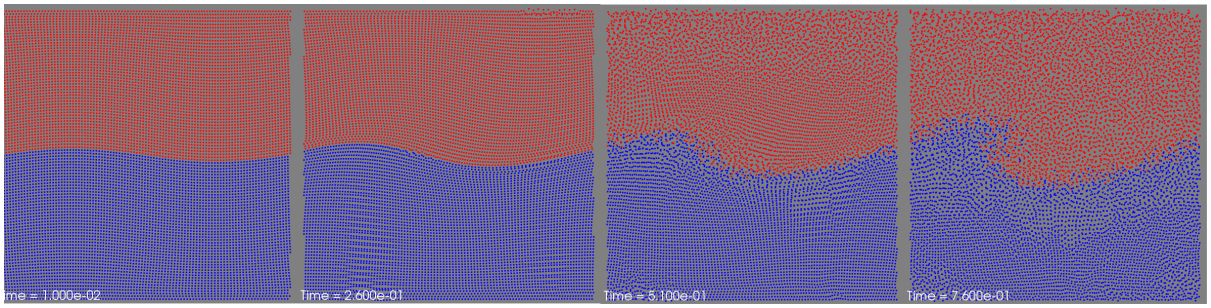

Figure 6.12: KHI interface evolution for $\rho_1/\rho_2 = 2$, $\sigma = 0$. Each frame is after a delay of $\Delta t = 0.25$

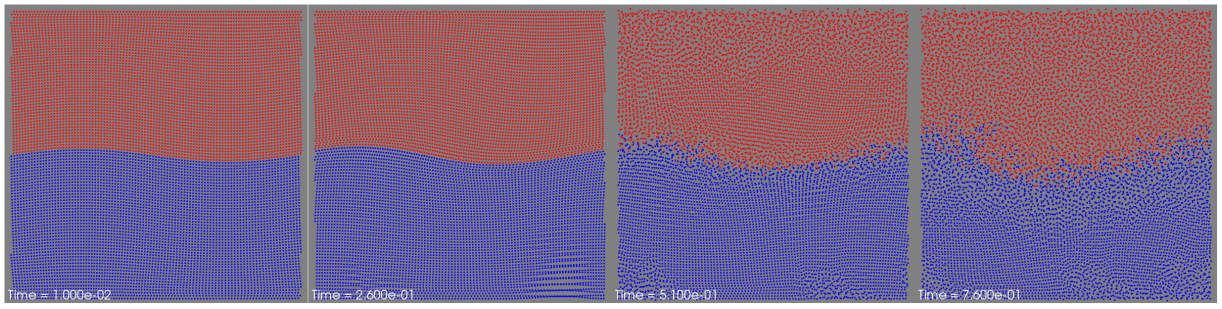

Figure 6.13: KHI interface evolution for $\rho_1/\rho_2 = 5$, $\sigma = 0$. Each frame is after a delay of $\Delta t = 0.25$

the three sets of simulations were run with $\nu = 5 \times 10^{-4}$. In cases with higher density, higher viscosity values are required to counter mixing.

6.3 Viscosity Stratified Flow

As mentioned in section 4.4, both, pressure-driven and wall-driven channel flow can be unstable to arbitrarily small values of Re in the presence of a viscosity discontinuity [27]. Similar to KHI, the growth of the instability is exponential at first. Linear stability analysis can be performed in this region, i.e. second and higher order perturbation terms can safely be neglected, therefore, this is sometimes known as the linear growth regime. As the amplitude of the disturbance starts increasing, the higher order terms can no longer be neglected and the system is said to be in the non-linear growth regime. The growth is no longer exponential.

Our interest lies in understanding the behaviour of the system in the non-linear regime. In order to validate the code, we compare our results with those in existing literature in

the linear regime.

6.3.1 Small Domain Trial

The surface tension model and the viscosity model are both diffused interface models. The properties are not treated to have sharp jumps at the interface, but as if they were smoothed out over a distance of a few Δx. It is therefore important to have a good particle resolution near the interface. As we are not interested in the dynamics near the walls, we consider only a thin region surrounding the interface for the simulation.

Figure 6.14 shows the domain being considered. It has a height of 0.4 unit, the wavelenght introduced is same as the width, which is 1 unit. The interface is at the middle. The domain is periodic in x-direction and is bounded by moving walls in the y-direction. We wish to simulate a problem where the height of the actual domain is 1 unit, so the velocity field is set up according to the height = 1 unit case, as shown in figure 6.15. The walls are given velocity equal to that of the fluid layer in contact, and a no-slip condition is used. The choice of slip or no-slip is inconsequential as there is no relative velocity between the wall and the fluid either way.

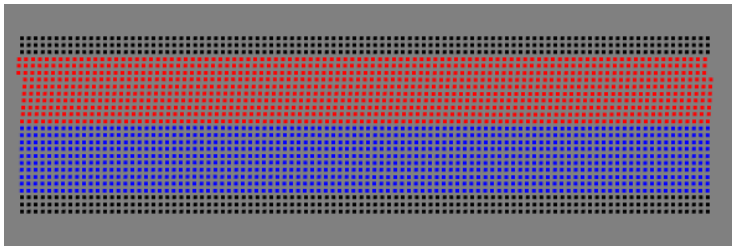

Figure 6.14: Small domain setup

Re based on the net flow rate, higher viscosity value and the domain height we are trying to simulate (height = 1 unit) is set to be 100. The particle spacing, Δx, is 0.01. Timestep values, Δt were 10^{-4} unit.

The goal of this experiment was the check the significance of boundary effect due to the walls on the growth rates. Three inital perturbation amplitudes, namely 2.5×10^{-3} unit, 5×10^{-3} unit and 10×10^{-3} unit were used. Figures 6.16a, 6.16b and 6.16c show the variation of perturbation amplitude with time for the three respective cases. It is seen that irrespective of the initial perturbation magnitude, the perturbations die out.

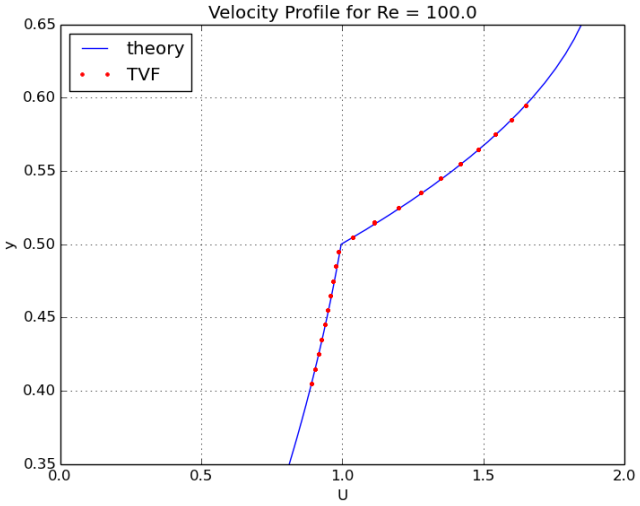

Figure 6.15: Small domain u-velocity profile

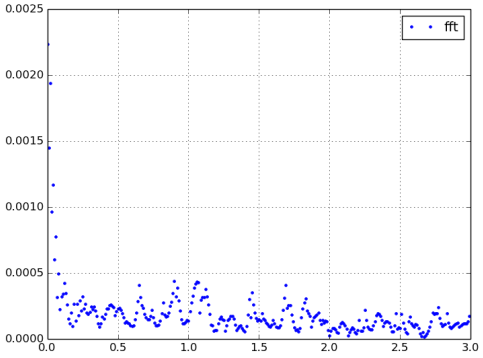

(a) $a_0 = 2.5 \times 10^{-3}$

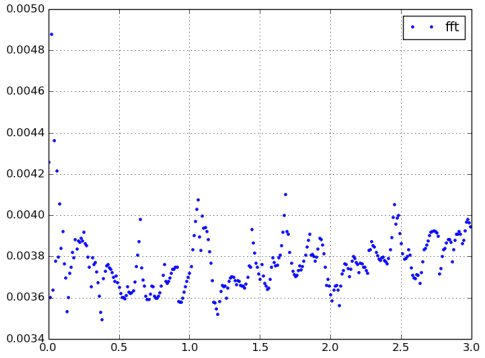

(b) $a_0 = 5 \times 10^{-3}$

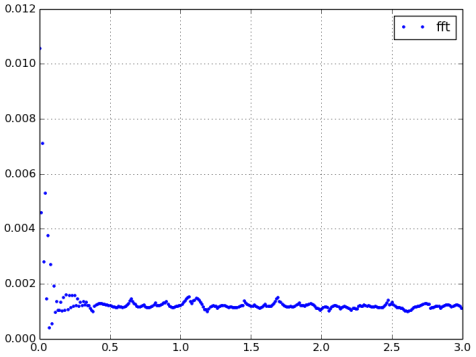

(c) $a_0 = 10 \times 10^{-3}$

Figure 6.16: Growth of instability (amplitude vs. time) in a small domain with different initial perturbation amplitudes

The boundary effect is significant even in case of low amplitude perturbations. Hence, simulations need to be carried out in domains with heights comparable to the wavelength.

6.3.2 Problem Setup

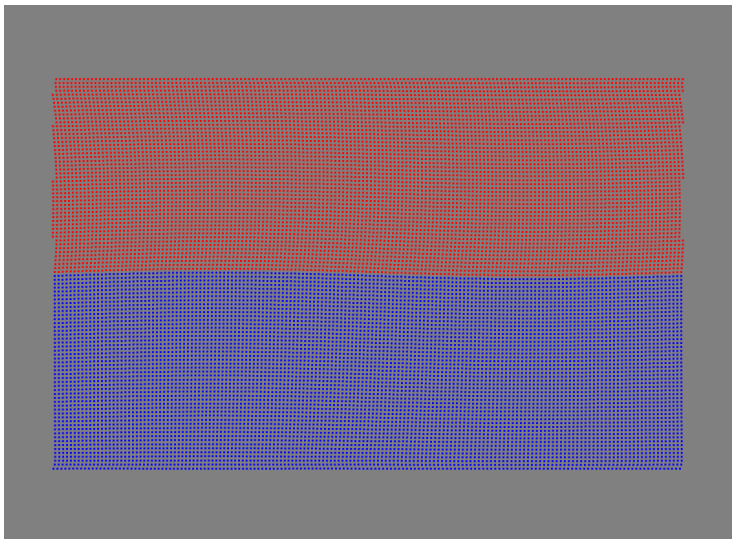

Figure 6.17: Viscosity Stratification setup

The problem is as defined in subsection 2.1.2. The same is shown in here in figure 6.17. The different coloured particles represent the two fluids. They are bounded by two stationary solid walls. The domain is periodic in the x-direction (direction of flow) in order to recreate an infinite domain. There is a small sinusoidal perturbation of the interface at $t = 0$. We are solving a pressure-driven flow here. A uniform body force is used to recreate the uniform pressure gradient. As described in subsection 2.1.2 the particles are initialised with u-velocity profiles of a stable poiseuille flow. This is the base flow, and the perturbations will grow over this.

The interparticle spacing, Δx, is 0.01 unit for both, the fluid and the wall. The bottom wall has 3 particle layers, and the top wall has 4 particle layers (the fourth layer is redundant and may be done away with). The same particle resolution is used throughout unless otherwise mentioned.

Figure 6.17 shows a fluid domain of $width = 1.6$ unit and $height = 1$ unit. The perturbation wave hence has a wavelength of 1.6 unit. Differently sized domains were used for the different wavelength cases simulated in subsection 6.3.3.

Choice of the kernel and kernel smoothing length are the same as they were in the KHI cases.

6.3.3 Large Initial Perturbation

Sahu et al. [33] have numerically solved the Orr-Sommerfeld equations for a pressure-driven channel flow. They have done the analysis for the interface of a Newtonian and a Herschel-Bulkley fluid. Herschel-Bulkley models are used for incorporating the presence of a yield stress along with power law behaviour of a fluid. As a special case of a Herschel-Bulkley/Newtonian interface, results for a Newtonian/Newtonian interface are also presented.

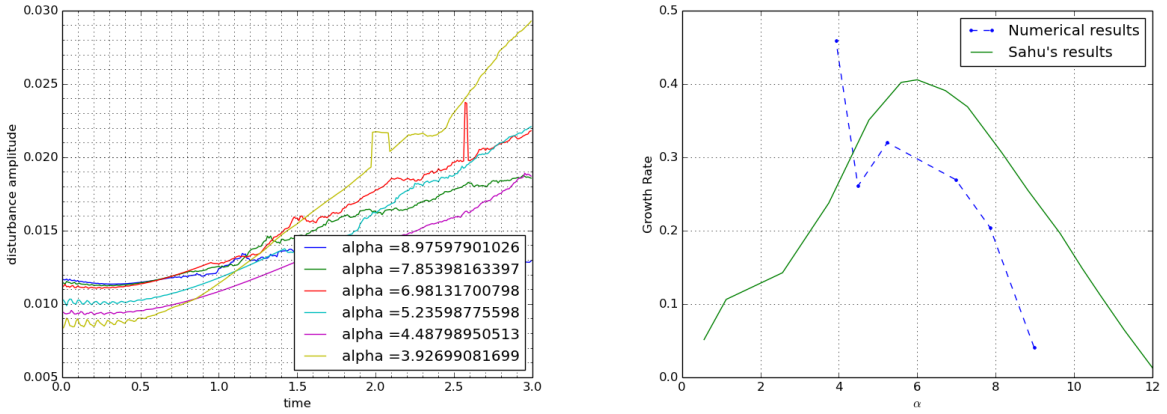

(a) Amplitude vs. time

(b) Growth vs. α

Figure 6.18: Without forced perturbation

Two types of initialisations were attempted. The first one is the standard initialisation found in literature where simply the interface is perturbed. The second one is forcing the interfacial perturbation as described in section 5.5.

Figure 6.18 shows the growths and the growth rates across different wavelengths for the simple interfacial perturbation case. α is the wavenumber given by $\alpha = 2\pi/\lambda$, where λ is the wavelenght. Figure 6.18b shows the obtained growth rates and the growth rates reported by Sahu. We see that while the rates are in the same ballpark as those reported by Sahu the values are off by at least 15%. The cause of this mismatch was suspected to be the inconsistent initialisation. Also, from figure 6.19a we can see that there are initial

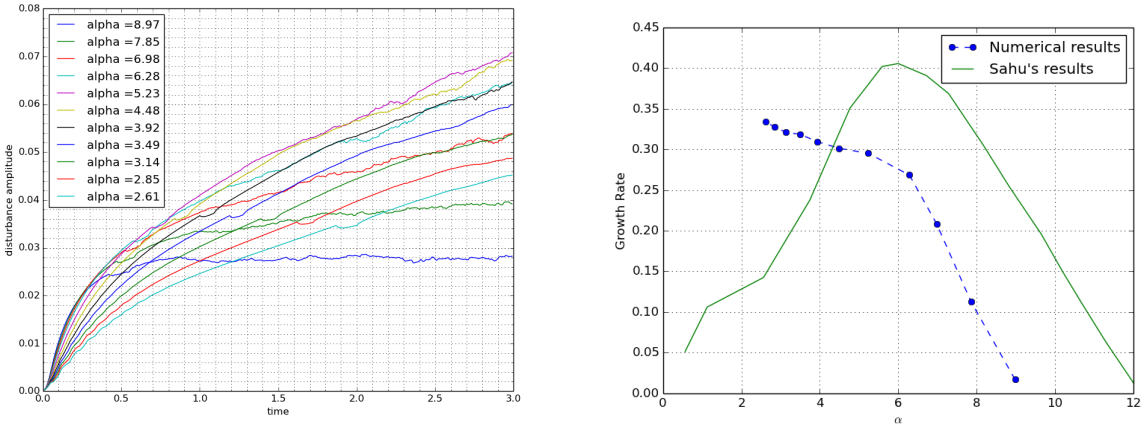

(a) Amplitude vs. time

(b) Growth vs. α

Figure 6.19: With forced perturbation

oscillations in the amplitude of the wave. These osciallations are also a manifestation of the incorrect initialisation as is explained in greater detail in subsection 5.1.1.

The forced perturbation method of initialisation was tried. The results for the same are presented in figure 6.19. Once again, while the results are in the same ballpark and follow an approximate trend the values are off by at least 15%. This is once again due to initialisation that is inconsistent with Sahu's initialisation.

6.3.4 Small Initial Perturbation

In order to resolve the problem of inconsistent or incorrect initialisation in these problems, we considered the work of Prasad et al. [28]. Prasad et al. have solved a simpler system of Newtonian fluids with a front-tracking/finite difference method. Prasad et al. have reported an exponential growth starting at almost $t = 0$ when the problem is initialised with a very small initial perturbation (5×10^{-4} unit).

We attempted to reproduce a representative growth curve from this work. The initial perturbation amplitude is 5×10^{-4} unit, that is over two orders smaller than the perturbation used in the earlier case (subsection 6.3.3). The size of the box is $1 \times 1\text{unit}^2$, and the wavelength is half the box width, i.e. $\lambda = 0.5$ unit. Height of the two layers is different, the lower layer being 4 times taller (see figure 6.20). The Reynolds number, Re, is based on the interface velocity, higher viscosity value and the domain height (expressions

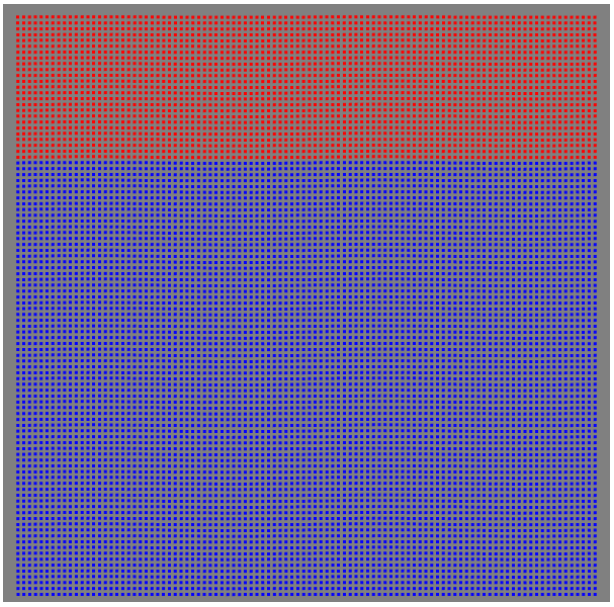

Figure 6.20: Problem setup for small initial perturbation; thickness ratio $(n) = 4$, viscosity ratio $(m) = 0.5$, $Re = 7.1$, $\lambda = 0.5$

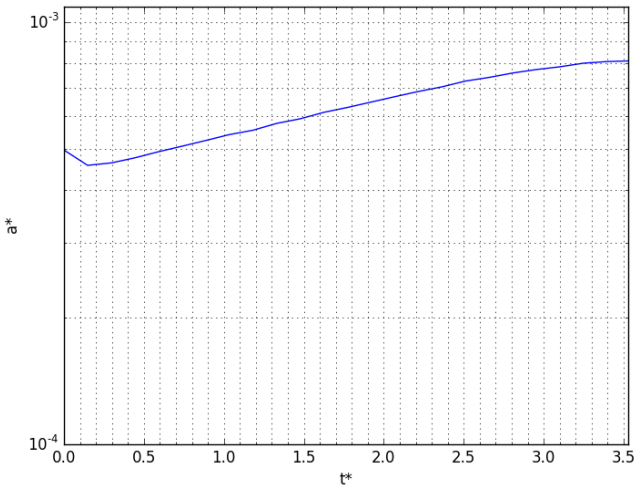

Figure 6.21: Growth curve for small amplitude initial perturbation

for Re and the initial u-velocity have been provided in [28]).

The growth rate, i.e. slope of the straight line in figure 6.21, obtained for this case is 0.174 and the one reported by Prasad et al. is approximately 0.16 i.e. a 9% error.

Prasad et al. have used only two data points for validation of the code used. Moreover, one of the data points has a 20% error. This casts some doubt on the results produced by them.

Further, in the SPH simulations done here, the interface amplitude goes through an

initial oscillation. This is because the particle distribution used for initialising is not at equilibrium. The initial particle distribution begins with pressure waves which cause oscillation of the interfacial perturbation. This initial oscillation of the perturbation is also suspected to produce errors in the growth rates.

6.3.5 Viscosity Dependence

In order to check if the growth depended on the actual viscosities of the fluids and not just the viscosity ratio, m, or Re we ran tests with the same non-dimensional parameters but different actual values of viscosity. Kinematic viscosity of the lower fluid, ν_{low}, is varied from 5×10^{-1} unit to 10^{-3} unit.

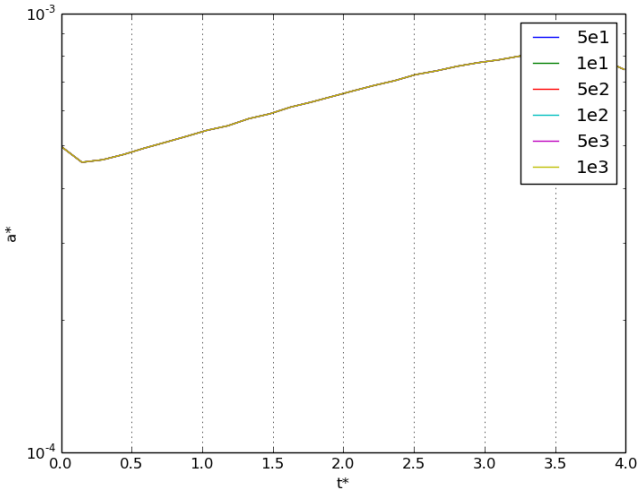

Figure 6.22: Viscosity stratified flow with small initial perturbation

Figure 6.22 shows that the different curves are identical and they are the same as the curve in figure 6.21. Only at higher time values we start seeing differences in the amplitudes. From figure 6.23 we can see that for $t^* > 8$ the curves start differing. This difference can be attributed to particle mixing. By this time ($t^* = 8$) the interface is well past the linear regime and the two phases have started mixing.

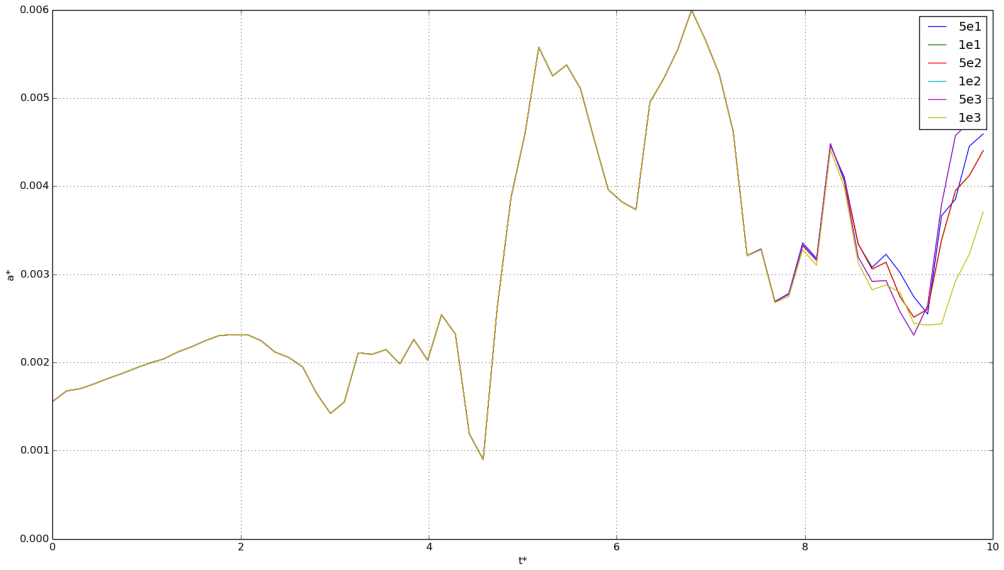

Figure 6.23: Growth of perturbation for various viscosity values

6.4 Conclusions

The study set out to explore the use of SPH for understanding the physics of core-annular flows. The interface in these cases is often unstable and wavy. We attempted to capture the material and flow discontinuities using state of the art SPH formulations. SPH has clear advantages in handling compressible flows, free surface flows and moving geometries. It has not been used extensively with internal, incompressible flows. Moreover, the specific class core-annular flows has not been touched by SPH at all. We sought to answer the question of how good SPH currently is at handling these problems.

In the course of this work we identified a few issues in current practices employed in CFD analyses of fluid instabilities. Stability problems are sensitive to the initialisation and it must be carefully handled. In easier problems it is possible to initialise the problem exactly, but in most problems an exact initialisation is not available. We attempted to device a universal initialisation scheme but it has its own limitations.

Due to interfacial instabilities, the SPH particles tend to mix. In this work along with surface tension, viscosity was used in order to reduce interfacial noise and maintain immiscibility. A better, physically consistent way of enforcing immiscibility is required.

Better surface tension implementations may be explored for the same.

While the SPH formulations tested were capable of handling discontinuities in base flow where the particles were well ordered and the interface was smooth, they performed poorly in situations with high particle disorder especially when it is close to the interface.

Viscosity-stratification has not been dealt with in SPH so far. We attempted a naive implementation in this thesis and tested it for simple cases but it requires thorough testing and improvements.

Current state of the art in SPH has certain limitations with respect to handling stratified flows. Overcoming these limitations will allow us to exploit all the advantages of SPH in flow problems traditionally handled using grid based schemes.

Appendix A

KHI Linear Stability Analysis

A.1 Linear Stability Analysis

The simplified analysis of the KHI instability is presented here. Two inviscid fluids are considered flowing over each other in a domain with infinite depth and height. Kelvin's circulation theorem holds in this case. We assume that there is no rotational perturbation at the start, therefore, the fluids remain irrotational. The analysis is further restricted to incompressible flows, so that a velocity potential may be assumed in the two phases.

The sinusoidal interface perturbation is represented by the function $\zeta(x,t)$, given by

$$\zeta(x,t) = \zeta_0 \exp[i(kx - \omega t)], \tag{A.1}$$

where k is real. Thus, $\zeta(x,t)$ is periodic in the x direction. The dynamic boundary condition at the interface is that the pressure across the interface should remain continuous, i.e. $p_1 = p_2$ (in the absence of surface tension). The kinematic boundary condition is that the vertical velocity of the two fluids at the interface should be equal to the rate of motion of the interface itself, i.e. no cavitation or penetration at the interface. Potential flow with the given perturbation under the said kinematic and dynamic boundary condition gives us a condition on ω [34][17]

$$\frac{\omega}{k} = \frac{\rho_1 U_1 + \rho_2 U_2}{\rho_1 + \rho_2} \pm \sqrt{-\frac{\rho_1 \rho_2 (U_1 - U_2)^2}{(\rho_1 + \rho_2)^2} + \frac{g}{k}\frac{\rho_2 - \rho_1}{\rho_1 + \rho_2}}. \tag{A.2}$$

In the presence of surface tension, the dynamic boundary condition takes the form $p_1 - p_2 = \sigma\zeta_0 k^2$, see (3.1). In this case (A.2) becomes

$$\frac{\omega}{k} = \frac{\rho_1 U_1 + \rho_2 U_2}{\rho_1 + \rho_2} \pm \sqrt{-\frac{\rho_1\rho_2(U_1 - U_2)^2}{(\rho_1 + \rho_2)^2} + \frac{g}{k}\frac{\rho_2 - \rho_1}{\rho_1 + \rho_2} + \frac{\sigma k}{\rho_1 + \rho_2}}. \tag{A.3}$$

From (A.1) it is clear that the perturbation will grow if ω is imaginary. Therefore, for stability we require

$$-\frac{\rho_1\rho_2(U_1 - U_2)^2}{(\rho_1 + \rho_2)^2} + \frac{g}{k}\frac{\rho_2 - \rho_1}{\rho_1 + \rho_2} + \frac{\sigma k}{\rho_1 + \rho_2} \geq 0, \tag{A.4}$$

which can be simplified to

$$\frac{\rho_1 + \rho_2}{k\rho_1\rho_2(U_1 - U_2)^2}\left(g(\rho_2 - \rho_1) + k^2\sigma\right) \geq 1. \tag{A.5}$$

A.1.1 Comments

The LHS of (A.5) is known as *Richardson Number* (*Ri*). It is defined as the ratio of potential energy to kinetic energy. Once again, we can see that KHI is essentially a struggle between the kinetic energy of the velocity difference of the fluids, and the two components of potential energy, viz. gravitational potential energy which comes from raising the denser fluid against gravity and surface energy which is an effect of increasing the interfacial surface area against surface tension. Given enough kinetic energy to begin with, the interface will be unstable.

Equation (A.5) gives other insights into the phenomenon:

- In the absence of surface tension (i.e. $\sigma = 0$), for a large enough k the interface is unstable. In other words, the interface is unconditionally unstable to short waves.
- If the fluid on top is heavier (i.e. $\rho_1 > \rho_2$), we may get an unstable interface. Further if the velocities are made equal, then it is a case of pure Rayleigh–Taylor instability.
- In case of a stable interface, depending on the densities the expression gives us internal gravity waves or surface waves.

Appendix B

The PySPH Framework

Throughout the course of this thesis we have used PySPH [35][36] (versions 1.0a1, 1.0a2 and pre-release versions) for setting up and running the simulations. PySPH is a Python based, free and open-source framework for SPH simulations.

All the particles in the domain do not interact with all other particles, at any given time each particle interacts with particles that come within a certain radius. These particles are known as 'neighbour particles'. At each time step we must identify the 'neighbours' for all of the particles, and the ODEs are evolved in time by considering particle interactions only among neighbours. PySPH handles all the back-end work of managing the neighbour searches, kernel value calculations, evolution of properties and dumping of data. The user only needs to define the governing equations and the initial problem setup. Also, the standard SPH equations a used in this work were predefined in PySPH, ready for use.

PySPH also has a visualisation tool, all the images of particles, velocity and colour field etc. in this thesis have been generated using the same.

Appendix C

SPH Stability Analysis

SPH was initially developed for application in compressible gas systems where pressure always remained positive. The inherent versatility of SPH led to its use in solving several problems where there is a possibility of negative stresses. Swegle (1995) [37] was the first to study an instability in some such cases. Particles were seen to clump together in pairs, the cause was attributed to negative stresses and the nature of the second derivative of the kernel function. This 'tensile instablity' was further studied by Morris [14][38]. Morris suggested changes in the kernel function to achieve stability. The instability has also been seen in cases where the stresses always remained positive. Monaghan [39] suggested a small change to the SPH formulation by adding an artificial stress term for correcting the instability.

As explained earlier, SPH equations are equations describing inter-particle forces, these equations generally form action-reaction pairs and subsequently linear momentum is conserved in the system. When the pressures become negative, particles start attracting each other. Normally when particles move close to each other, the density at those particles rises which translates to a rise in pressure and the particles repel each other, but due to the nature of SPH, it is possible that even when two particles move very close to each other the densities do not increase sufficiently. Here, the particles will continue to attract each other and will eventually end up in an inseparable pair.

C.1 Source of Instability

Here is a simplified problem in 1D for understanding the source of the instability. Similar analyses have been done by Morris [14] for more complicated formulations in 2D and 3D and with added complications such as non uniform particle spacing, etc.

C.1.1 Formulation

As mentioned earlier, the instability is seen in cases where the SPH formulation conserves momentum exactly. Morris has studied it in depth for a magneto-hydrodynamics problem, in simple fluid dynamics the implementation takes the form:

$$\frac{dv_a}{dt} = -\sum_b m_b \left(\frac{p_a}{\rho_a^2} + \frac{p_b}{\rho_b^2} \right) \frac{\partial W_{ab}}{\partial x_a} \tag{C.1}$$

$$\rho_a = \sum_b m_b W_{ab} \tag{C.2}$$

$$p_a = c^2(\rho_a - \rho_0 + \rho_0 \Re) \tag{C.3}$$

Here $c^2\rho_0\Re$ is the 'background pressure', clearly, if $\Re > 0$, then p_a may remain positive under small oscillations, but if $\Re < 0$, then p_a may become negative.

C.1.2 Linearisation of Equations

Morris has studied the dispersion relation for sound waves propagating in one-dimension. Consider an infinite row of uniformly spaced particles with equal masses oscillating about their mean, their motion may be described by

$$x_a = a\Delta x + Xe^{i\phi} \tag{C.4}$$

$$v_a = Ve^{i\phi} \tag{C.5}$$

$$\rho_a = \rho_0 + Re^{i\phi} \tag{C.6}$$

with

$$\rho_0 = m \sum_b W_{ab} \tag{C.7}$$

C.1.3 Dispersion Relation

The equations (2.29) through (C.3) are linearised by substituting (C.6) and ignoring the higher order terms. On further simplification we are left with a dispersion relation, which relates the frequency of the vibration to the wavelength. If an even kernel is assumed, the dispersion relation boils down to

$$\omega^2 = \frac{2mc^2\Re}{\rho_0} \sum_j (1 - \cos k\Delta x j) \frac{\partial^2 W_{ab}}{\partial x^2} + \left(\frac{mc^2}{\rho_0}\right)(1 - 2\Re) \left\{ \sum_j \sin k\Delta x j \frac{\partial W_{ab}}{\partial x} \right\}^2 \tag{C.8}$$

C.1.4 Numerical Speed of Sound

The analytical dispersion relation for sound waves is

$$\omega^2 = c^2 k^2 \tag{C.9}$$

We can define the numerical speed of sound on similar lines as

$$c_{num}^2 = \frac{\omega^2}{k^2} \tag{C.10}$$

We want c_{num} to be as close to c as possible, if c_{num}^2 becomes negative then the solution is no longer a travelling wave but an exponentially growing or decaying perturbation. Thus,

$$c_{num}^2 \begin{cases} \geq 0, & \text{Stable} \\ < 0, & \text{Unstable} \end{cases} \tag{C.11}$$

C.1.5 Results

The shortest wavelength, λ_{min}, capable of being resolved by a discrete system is $2\Delta x$. This wavelength is also reported to become unstable the earliest. Thus, we expect $k \approx \pi/\Delta x$

to be unstable. On substituting this in (C.8) we are left with

$$\omega^2 = \frac{2mc^2\Re}{\rho_0} \sum_{j=-\infty}^{\infty} (1 - \cos \pi j) \frac{\partial^2 W_{ab}}{\partial x^2}(j\Delta x, h) \tag{C.12}$$

If we are using a kernel with compact support, like the cubic spline, then the kernel derivative will drop to 0 for $x > 2h$. For a simple case where $W_{ab} = 0$ for $x > 2\Delta x$ (i.e. $h < 1.5\Delta x$), we are left with only two terms in the summation and they correspond to $j = \pm 1$, we get

$$\omega^2 = \frac{8mc^2\Re}{\rho_0} \frac{\partial^2 W_{ab}}{\partial x^2}(\Delta x, h) \tag{C.13}$$

We need positive ω^2 for stability as shown earlier (C.11), therefore, W'' must change sign with $\Re$ which represents the background pressure (C.3). So, when $\Re$ is 0, W'' must be 0 at the nearest neighbour. This can be achieved by using an appropriate smoothing length, for eg., in a Gaussian kernel, $W'' = 0$ for $h = \sqrt{2}\Delta x$.

C.2 Conclusions

Several ways of dealing with the instability have been suggested, some of them are

- Careful selection of the particle spacing and the smoothing length.
- Using modified kernels, such as the one suggested by Morris which is composed of a series of kernels, he calls this a 'pack of camels' eliminates the instability.
- Introduction of an artificial viscosity does not eliminate the instablity, though it does reduce its growth rate.
- Another easy approach of dealing with the instability is to use the correction suggested by Monaghan[39] which introduces an artificial stress term.
- Using a formulation which employs the difference of the stresses also gives stable results

$$\frac{dv_a}{dt} = -\sum_b m_b \left(\frac{p_a - p_b}{\rho_a \rho_b} \right) \frac{\partial W_{ab}}{\partial x_a} \tag{C.14}$$

In such a formulation $\Re$ doesn't appear in the dispersion relation at all, but this form doesn't conserve momentum exactly.

In general, it is important to understand the pitfalls of the formulation being employed as the stability and accuracy of each formulation is sensitive to a number of parameters like the smoothing length, the background pressure, the speed of sound, the particle arrangement and the particle spacing.

Bibliography

[1] A Bensakhria, Y Peysson, and G Antonini. Experimental study of the pipeline lubrication for heavy oil transport. *Oil & gas science and technology*, 59(5):523–533, 2004.

[2] Rama Govindarajan and Kirti Chandra Sahu. Instabilities in viscosity-stratified flow. *Annual Review of Fluid Mechanics*, 46:331–353, 2014.

[3] Daniel J Price. Modelling discontinuities and Kelvin–Helmholtz instabilities in SPH. *Journal of Computational Physics*, 227(24):10040–10057, 2008.

[4] Mostafa Safdari Shadloo and M Yildiz. Numerical modeling of Kelvin–Helmholtz instability using smoothed particle hydrodynamics. *International Journal for Numerical Methods in Engineering*, 87(10):988–1006, 2011.

[5] Mostafa Safdari Shadloo and Mehmet Yıldız. Kelvin–Helmholtz instability by SPH. ECCOMAS, 2011.

[6] Rouhollah Fatehi, Mostafa Safdari Shadloo, and Mehrdad T Manzari. Numerical investigation of two-phase secondary kelvin–helmholtz instability. *Proceedings of the Institution of Mechanical Engineers, Part C: Journal of Mechanical Engineering Science*, 228(11):1913–1924, 2014.

[7] Robert A Gingold and Joseph J Monaghan. Smoothed particle hydrodynamics: theory and application to non-spherical stars. *Monthly notices of the royal astronomical society*, 181(3):375–389, 1977.

[8] Joe J Monaghan. Smoothed particle hydrodynamics. *Annual review of astronomy and astrophysics*, 30:543–574, 1992.

[9] Joe J Monaghan. Smoothed particle hydrodynamics. *Reports on progress in physics*, 68(8):1703, 2005.

[10] JI Read, T Hayfield, and O Agertz. Resolving mixing in smoothed particle hydrodynamics. *Monthly Notices of the Royal Astronomical Society*, 405(3): 1513–1530, 2010.

[11] S Adami, XY Hu, and NA Adams. A transport-velocity formulation for smoothed particle hydrodynamics. *Journal of Computational Physics*, 241:292–307, 2013.

[12] S Adami, XY Hu, and NA Adams. A new surface-tension formulation for multi-phase SPH using a reproducing divergence approximation. *Journal of Computational Physics*, 229(13):5011–5021, 2010.

[13] J Bonet and S Kulasegaram. Correction and stabilization of smooth particle hydrodynamics methods with applications in metal forming simulations. *International journal for numerical methods in engineering*, 47(6):1189–1214, 2000.

[14] Joseph Peter Morris. *Analysis of smoothed particle hydrodynamics with applications*. Monash University Australia, 1996.

[15] Joseph P Morris. Simulating surface tension with smoothed particle hydrodynamics. *International Journal for Numerical Methods in Fluids*, 33(3):333–353, 2000.

[16] JU Brackbill, Douglas B Kothe, and C1 Zemach. A continuum method for modeling surface tension. *Journal of computational physics*, 100(2):335–354, 1992.

[17] PK Kundu and IM Cohen. Fluid mechanics, 759 pp, 2004.

[18] Vinesh H Gada and Atul Sharma. On derivation and physical interpretation of level set method–based equations for two-phase flow simulations. *Numerical Heat Transfer, Part B: Fundamentals*, 56(4):307–322, 2009.

[19] XY Hu and Nikolaus A Adams. A multi-phase SPH method for macroscopic and mesoscopic flows. *Journal of Computational Physics*, 213(2):844–861, 2006.

[20] Mingyu Zhang. Simulation of surface tension in 2d and 3d with smoothed particle hydrodynamics method. *Journal of Computational Physics*, 229(19):7238–7259, 2010.

[21] Mingyu Zhang, Shudao Zhang, Hui Zhang, and Lili Zheng. Simulation of surface-tension-driven interfacial flow with smoothed particle hydrodynamics method. *Computers & Fluids*, 59:61–71, 2012.

[22] G Ooms, C Vuik, and P Poesio. Core-annular flow through a horizontal pipe: hydrodynamic counterbalancing of buoyancy force on core. *Physics of Fluids (1994-present)*, 19(9):092103, 2007.

[23] Mihai Basa, Nathan J Quinlan, and Martin Lastiwka. Robustness and accuracy of SPH formulations for viscous flow. *International Journal for Numerical Methods in Fluids*, 60(10):1127–1148, 2009.

[24] MB Liu and GR Liu. Smoothed particle hydrodynamics (SPH): an overview and recent developments. *Archives of computational methods in engineering*, 17(1):25–76, 2010.

[25] S Adami, XY Hu, and NA Adams. A generalized wall boundary condition for smoothed particle hydrodynamics. *Journal of Computational Physics*, 231(21): 7057–7075, 2012.

[26] Paul W Cleary and Joseph J Monaghan. Conduction modelling using smoothed particle hydrodynamics. *Journal of Computational Physics*, 148(1):227–264, 1999.

[27] Chia-Shun Yih. Instability due to viscosity stratification. *Journal of Fluid Mechanics*, 27(02):337–352, 1967.

[28] Qing Cao, Kausik Sarkar, and Ajay K Prasad. Direct numerical simulations of two-layer viscosity-stratified flow. *International journal of multiphase flow*, 30(12): 1485–1508, 2004.

[29] Oscar Agertz, Ben Moore, Joachim Stadel, Doug Potter, Francesco Miniati, Justin Read, Lucio Mayer, Artur Gawryszczak, Andrey Kravtsov, Åke Nordlund, et al.

Fundamental differences between SPH and grid methods. *Monthly Notices of the Royal Astronomical Society*, 380(3):963–978, 2007.

[30] DI Pullin. Numerical studies of surface-tension effects in nonlinear Kelvin–Helmholtz and Rayleigh–Taylor instability. *Journal of Fluid Mechanics*, 119:507–532, 1982.

[31] RH Rangel and WA Sirignano. Nonlinear growth of Kelvin–Helmholtz instability: effect of surface tension and density ratio. *Physics of Fluids (1958-1988)*, 31(7): 1845–1855, 1988.

[32] RH Rangel and WA Sirignano. The linear and nonlinear shear instability of a fluid sheet. *Physics of Fluids A: Fluid Dynamics (1989-1993)*, 3(10):2392–2400, 1991.

[33] KC Sahu, P Valluri, PDM Spelt, and OK Matar. Linear instability of pressure-driven channel flow of a Newtonian and a Herschel-Bulkley fluid. *Physics of Fluids (1994-present)*, 19(12):122101, 2007.

[34] Philip G Drazin and William Hill Reid. *Hydrodynamic stability*. Cambridge university press, 2004.

[35] Prabhu Ramachandran and Kunal Puri. PySPH: A framework for parallel particle simulations. In proceedings of the 3rd International Conference on Particle-Based Methods (Particles 2013), Stuttgart, Germany, 18th September, 2013.

[36] PySPH developers. PySPH documentation. URL `http://pysph.readthedocs.org/en/latest/index.html`. [Online; retrieved 26-Jun-2015].

[37] JW Swegle, DL Hicks, and SW Attaway. Smoothed particle hydrodynamics stability analysis. *Journal of computational physics*, 116(1):123–134, 1995.

[38] Joseph Peter Morris. A study of the stability properties of SPH. *arXiv preprint astro-ph/9503124*, 1995.

[39] Joseph J Monaghan. SPH without a tensile instability. *Journal of Computational Physics*, 159(2):290–311, 2000.

Acknowledgements

I take this opportunity to thank Prof. Bhattacharya and Prof. Prabhu for investing so much time in me. They have patiently guided me through the slowest phases of my work. Through them I have learnt a lot about fluid mechanics, and research in general. I would also like to thank Kunal Puri for helping me out whenever I got stuck, and even doing parts of my work when I was unable to.

Almost all of my work was done using PySPH, an open source framework for SPH simulations. I would like to thank Prof. Prabhu, Kunal, the other developers and everyone else who has contributed to the project. I am thankful to Prof. Bhattacharya for providing me an excellent lab space and a machine. It made working much easier.

Directly or indirectly, my friends have been constant sources of inspiration. Discussions with them, both academic and non-academic, have contributed to furthering my interest in science and learning. My sincere thanks to all of them. I would like to thank Neehar Jathar for providing the template for this thesis, it saved me a lot of crucial time.

I am deeply indebted to my parents for having faith in me, supporting me, and bearing with me all throughout. I cannot thank them enough.

Signature:  .....

Arpit Agarwal

10D100008

Date: 22 June 2015